Vortex lattice modelling of winglets on wind turbine blades

Døssing, Mads

Publication date:
2007

Document Version
Publisher's PDF, also known as Version of record

Risø-R-Report

Vortex Lattice Modelling of Winglets on Wind Turbine Blades

Mads Døssing

Risø-R-1621(EN)

Risø National Laboratory
Technical University of Denmark
Roskilde, Denmark
August 2007

Author: Mads Døssing
Title: Vortex Lattice Modelling of Winglets on Wind Turbine Blades
Departments: Wind Energy Department - Risø & Department of Mechanical Engineering - DTU

3rd version. 18 oct. 2007

Risø-R-1621(EN)
Mek-FM-EP 2007-04
August 2007

Abstract:
The power production of wind turbines can be increased by the use of winglets without increasing the swept area. This makes them suitable for sites with restrictions in rotor diameter and in wind farms. The present project aims at understanding how winglets influences the flow and the aerodynamic forces on wind turbine blades. A free wake vortex lattice code and a fast design algorithm for a horizontal axis wind turbine under steady conditions has been developed. 2 winglet designs are threated in detail.

ISSN 0106-2840
ISBN 978-87-550-3633-8

Information Service Department
Risø National Laboratory
Technical University of Denmark
P.O.Box 49
DK-4000 Roskilde
Denmark
Telephone +45 46774004
bibl@risoe.dk
Fax +45 46774013
www.risoe.dk

Summary

The power production of wind turbines can be increased by the use of winglets without increasing the swept area. This makes them suitable for sites with restrictions in rotor diameter and in wind farms.

The present project aims at understanding how winglets influences the flow and the aerodynamic forces on wind turbine blades.

A free wake vortex lattice code and a fast design algorithm for a horizontal axis wind turbine under steady conditions has been developed.

2 winglet designs are threated in detail.

Resumé

Vindmøllers energi-produktion kan øges ved brug af en winglet, uden at det bestrøgne areal øges. Dette gør dem egnede til brug på anlæg, hvor der er restriktioner på rotorens diameter.

Formålet med nærværende projekt er at opnå en forståelse for, hvorledes en winglet påvirker strømningnen og krafterne på en vindmølle vinge.

En vortex-lattice kode og en hurtig design algoritme er blevet udviklet for en horisontal mølle under tidsuafhængige forhold.

2 winglet design er behandlet i detaljer.

Preface

This thesis was prepared at the Wind Energy Department at Risø in collaboration with the Department of Mechanical Engineering, the Technical University of Denmark in partial fulfillment of the requirements for acquiring the M.Sc. degree in engineering.

The thesis deals with different aspects of mathematical and numerical modeling of wind turbine aerodynamics. The main focus is on development of methods for prediction the performance of turbine blades with winglets.

I thank my supervisors Mac Gaunaa and Robert Flemming Mikkelsen for their aid and support.

Kongens Lyngby, August 2007

Mads Døssing

Contents

Part 1

Introduction

The present report describes the mathematical methods and the results obtained regarding winglets mounted on windturbines. The main emphasis is on the aerodynamics and the associated forces, thus neglecting any elastic behavior of the blades. Efficient mathematical models for simulation of winglets on turbines were not available at the beginning of this project and the original idea was to make Vortex Lattice simulations in order to study the physical properties. Severe shortcomings of the method soon appeared and this project evolved into a study of numerical methods and the general properties of winglets. Eventually a modified Vortex Lattice method was used for simulation and a nearwake design method was developed which is considered more accurate.

1.1 Motivation

Winglets increases the efficiency of wind turbine rotors by increasing the power production for a given blade length, making them attractive on sites with design restrictions on the rotor radius. On sites without restrictions the easiest way to increase the power is by using a longer traditional flat blade, but in wind farms this may have a negative impact on the total production due to the increased sweept area. Therefore, even if there are no design restrictions, winglets may still be attractive. Since a blade with a winglet is more expensive than a flat blade

and the manufacturing process is not well established, a clear understanding of the aeroelastic properties is needed in order for the industry to verify whether a production is profitable or not.

1.2 Winglet Description

Winglets are essentially extensions of the main wing. The cant, sweep and height describes the overall shape of a straight winglet, and the local shape is described by the chord, twist angle and 2D profile. The bend has a curve radius which is also important. The winglets threated in this work has zero sweep and cant angle, leaving the curve radius of the bend, the height and the twist and chord distribution as geometrical parameters. The chord and twist distribution are very important for the winglet efficiency and determining them is the aim of the design process. The winglet height can be considered a design parameter. The efficiency increases with height until the viscous drag outbalances the benefits of the winglet and usually there is an optimum winglet height around 3-4% of the blade length.

On airplanes the winglet works by decreasing the induced drag on the main wing. The induced drag is the component of lift in the direction opposite to the movement and despite its name it is therefore not associated with any viscous effects but instead to the change in inflow angle. On airplanes the inflow is angled down thereby tilting the force vector back. This change in the local inflow is caused by the complicated 3 dimensional nature of the wings where pressure variations redistributes the flow. On airplanes the change in flow is a velocity component, the downwash, perpendicular to the wing in the direction from the suction to the pressure side. One very visible effect is the tip vortex created by the pressure difference on the pressure and suction side of the wing which accelerates the air around the tip in a direction perpendicular to the wing. Traditionally the winglet has been seen as a device for decreasing this tip vortex. The principle is that by extending the wing the tip vortex is moved further away from the main blade and the strength of it is decreased, hence decreasing the downwash on the center parts of the wing where the aerodynamic forces are large. The wing can also be extended simply by increasing the span and this is actually more efficient aerodynamically since the force on the extra span adds to the lift. The downwash depends not only on the shape of the wing planform, the force distribution over the blade and winglet is also important.

The physics near wind turbine tips is essentially the same; a tip vortex is trailing off and generates a downwash on the blade. This tilts the local force vector in such a way that a force component, acting against the blade direction of rotation,

is created. On the main blade the direction of this unwanted downwash is against the incoming wind and this confuses matters because a well designed wind turbine already has a significant induction in this direction. I.e. 1/3 of the incoming wind under optimum conditions according to the theoretical Betz limit. However, even if the induction is less than desired the downwash will not contribute positively because a relatively small winglet creates only local effects, and will not alter the wake far downstream upon which the momentum theory and the Betz limit is based. This postulate, that the winglet acts locally is very important and will be threated in detail under the development of the design method. On the winglet itself the direction of the unwanted downwash is radial outward, and more generally the unwanted velocity component is termed normalwash. It is possible to generate a negative normalwash on the winglet, in which case a force component is created in the direction of rotation but the viscous drag may outbalance this. If the induced drag can be reduced it can have a relatively large effect on the torque generated by the blade because the reduction is mainly on the outer part. This is especially true if the blade is heavily loaded near the tip. It is therefore concluded that a reduction of induced drag is a primary concern. When the winglet is mounted the forces near the tip becomes larger and this in itself increases the power production and the thrust. Therefore, the winglet affects not only the induced drag but also the magnitude of all other aerodynamic forces near the tip. A design should therefore be evaluated on the power (C_p) and thrust coefficients (C_T) and not just the induced drag. An increase in C_p can be caused mainly by heavier loading near the tip, and not as much by a decrease in induced drag. This is associated with a large increase in C_T, and since the majority of thrust forces are concentrated near the tip the bending moments also increases substantially. In the winglet sense, it is better to design for a large reduction in induced drag with a small associated increase in thrust forces. The forces on the winglet itself does not contribute to the thrust. Besides from a positive or negative contribution to the total torque generated by the rotor the winglet induces a radial force and a twisting moment about the axis of the main blade. These forces are not threated in this work but are important for the aeroelastic behavior of the blade. Especially the twisting moment can be expected to be relatively large when compared to the existing twisting moments found in present turbine blades.

1.3 Overview of the Methods Applied

Because the winglet works by altering the flow and pressure properties it can be modeled using inviscous theory. It is important that the blade is not stalled, but in practice windturbines are often stalled near the root. Inviscid theory can therefore only to limited extend be applied to accurately predict the performance

of windturbines. The influence of winglets are confined to the outer parts of the blade where the assumption of inviscous flow is valid and inviscous theory can be used to study the local variations. The tip speed on turbines is limited to 70 m/s which is approximately 21% of the speed of sound which is well within the range of incompressible flow (¡ 30%). Locally, near the profile, the velocities can be much larger and the flow can not be considered incompressible. On the profile suction peak the local velocity can be as high as twice the incoming flow velocity. Despite of this the flow will be considered incompressible everywhere and potential theory will be used.

BEM and actuator disc methods can not predict variations in flow properties due to winglets and this leaves computational fluid dynamics (CFD) as the only established alternative. It is desirable to have a fast method for parameter studies and design validation and this is not the case with CFD. The available potential methods are roughly; 1) lifing line methods 2) Vortex Lattice methods 3) Panel methods. All 3 methods has been studied and all has been found to have weaknesses. The Vortex Lattice method is relatively slow and the induced drag forces are not easily evaluated. The panel method can accurately calculate the forces but long computational times makes it unusable. Both methods requires a wake model, and a Free Wake model has been implemented. It is difficult and time consuming to model the wake accurately and this adds to the uncertainty of the potential flow methods. The Vortex Lattice method was eventually chosen over the panel code. The lifting line method is simple and fast, and the accuracy is relatively good. It is different from the Vortex Lattice method in that the chord and twist distribution is not part of the solution. Instead the velocity and bound circulation distributions are found and an equivalent full 3D geometry can then be defined, something which is relatively simple as long as there is no substantial spanwise flow. From the velocity and circulation distribution it is also possible to evaluate all important forces. It is therefore clear that the velocity and circulation distribution describes the physics along the blade and the goal of the design process is to optimize these for a given geometry. Note that in viscous flow other non linear properties are important as well. Because the velocity and circulation distributions are so important the Vortex Lattice results are also converted to lifting line data, i.e. chordwise variations are neglected and the data is distributed along a line describing the span. This makes it easier to study different designs since data distributed over a Vortex Lattice surface are hard to interpret. It is also worth noticing that the forces evaluated along a lifting line includes the leading edge suction, something which requires special treatment in Vortex Lattice codes. To sum up, the final method consists of a Vortex Lattice computation of distributed velocities and circulation using a Free Wake model. Followed by transfer of data to a lifting line representation where forces are evaluated and results can compared to design input.

Despite a large effort the Vortex Lattice results were never really satisfactory,

something which is mainly due to the uncertainties of the wake model. Because of this and based on the experience gained a simpler model was made which is based on a known velocity and circulation distribution over a traditional flat blade. The task is then to extend the blade and circulation distribution in order to simulate a winglet and then predict the changes in velocities due to this. Under certain conditions it is only necessary to recalculate the influence of the wake immediately behind the blade and one quarter revolution downstream. This makes the algorithm fast and, because the wake is prescribed, the uncertainties of the free wake model is avoided. The circulation distribution is based on results for optimal designed wings, which is allowed as long as the changes in velocities along the blade is predicted correct. The method is used to design the winglets and predict the performance. Vortex Lattice simulations are used for validation.

The methods has been implemented in Matlab and Fortran. Practical considerations and source code has been completely left out of this report.

1.4 Outline of the Thesis

The contents of this thesis are presented in six parts.

Part 2 presents the applied potential flow theory. Coordinate systems and dimensionless variables are also introduced here.

Part 3 describes the lifting line method. The method is applied to wings in steady forward flight for which the optimum design of winglets can be found. The results are generalized to wind turbines.

Part 4 describes the free wake vortex lattice and panel method. The formulation applies to panel methods for which the Vortex Lattice method is a special case.

Part 5 describes the design process. Some important general issues regarding the choice of design parameters are discussed.

Part 6 discusses the predicted performance of 2 selected final winglet designs.

Part 7 contains conclusions.

Part 2

Theory

This part introduces coordinate systems, dimensionless variables and the applied theory for later reference.

2.1 Definition of Coordinate Systems

Two coordinate systems are defined as seen in Figure 2.1.

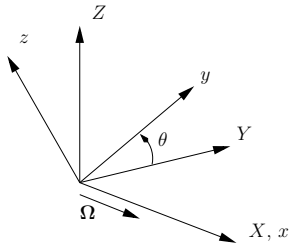

Figure 2.1: The initial and the rotating coordinate system.

The *initial coordinate system* corresponds to an earth reference frame. The

coordinates are denoted with capital letters.

$$\mathbf{R} = \{X, Y, Z\}^T$$

The *body coordinate system* is rotating about the X-axis of the initial system with the same rotational speed as the turbine rotor which is stationary in this frame of reference. The coordinates are denoted with small letters.

$$\mathbf{r} = \{x, y, z\}^T$$

The rotational speed is Ω and the motion is therefore completely described by the rotation vector $\mathbf{\Omega}$ defined in the initial coordinate system.

$$\mathbf{\Omega} = \{\Omega, 0, 0\}^T$$

2.2 Definition of Blade and Winglet Geometry

In the body fixed coordinate system the blade is positioned as shown in Figure 2.2. The radius is R. The winglet is extending downstream in the positive x-direction. The contour of the winglet is described by its height, h, and the curve radius of the bend ,R_c.

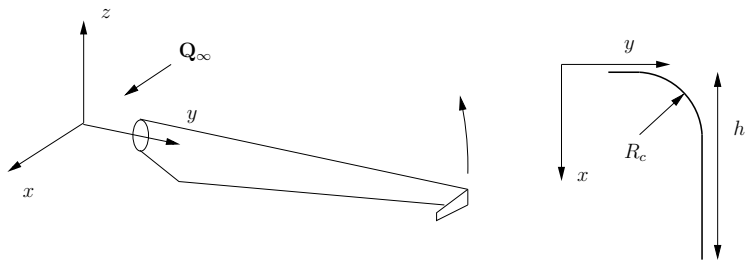

Figure 2.2: Definition of geometry. The winglet contour is shown to the right.

The twist, $twist_z$, and the chord, c, is described along the blade. Notice that a special definition of the twist is used, which is seen in figure 2.3.

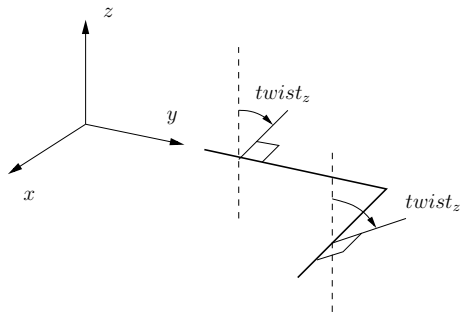

Figure 2.3: Definition of twist angle, $twist_z$.

2.3 Dimensionless Variables

Results will be presented in dimensionless form. Under the assumptions of linear theory and flow similarity the rules for scaling are given below. Coordinates are scaled by the turbine radius:

$\frac{y}{R}$ Spanwise coordinate

$\frac{x}{R}$ Downstream coordinate

$\frac{s}{R}$ Surface parameter along span

Velocities are scaled by the wind speed:

$\frac{u}{Q_\infty}$ x-velocity component

$\frac{v}{Q_\infty}$ y-velocity component

$\frac{w}{Q_\infty}$ z-velocity component

Tip speed ratio, thrust and power coefficients. Note that section C_p and C_T, usefull for describing the distribution of loads, will be defined in section 3.7.

$$\lambda = \frac{\Omega R}{Q_\infty}$$

$$C_p = \frac{M_x \Omega}{1/2 \rho Q_\infty^3 A}$$

$$C_T = \frac{F_x}{1/2 \rho Q_\infty^2 A}$$

The bound circulation can be scaled by the following relation which holds for wind turbines with similar flow. I.e. equal C_p, λ and geometrical contour.

$$\frac{\Gamma}{Q_\infty R} = Constant$$

2.4 Governing Equations

The following theory applies to an inviscid, irrotational and incompressible fluid, where a velocity potential, Φ can be defined

$$\nabla\Phi = \mathbf{Q}$$

The potential obeys Laplaces equation in both stationary and time dependent flows.

$$\nabla^2\Phi = 0 \tag{2.1}$$

2.5 The General Solution and Boundary Conditions

Equation (2.1) is a linear partial differential equations. Its general solution and boundary conditions are described below and forms the basis of all the applied mathematical techniques.

Boundary Conditions

For a body immersed in a fluid the boundaries are the body surface and infinity, and in general both Dirichlet and Neumann boundary conditions can be defined. The first condition is used in potential based panel methods where the potential is specified directly on the boundaries and the potential is solved for. The second is used in methods where a condition on the flow itself is specified on the boundary. The latter method is used in this work. The *first boundary condition* is tangential flow at the surface which can also be stated as zero normal flow

$$\text{BC1:} \quad (\mathbf{Q} - \mathbf{v}) \cdot \mathbf{n}|_{surface} = (\nabla\Phi - \mathbf{v}) \cdot \mathbf{n}|_{surface} = 0 \tag{2.2}$$

$\mathbf{n}$ is an outward pointing normal vector and $\mathbf{v}$ is the structural velocity. In the case of a rotating body this is

$$\mathbf{v} = \mathbf{\Omega} \times \mathbf{R}$$

The *second boundary condition* is that the disturbance of the body must vanish at infinity

$$\text{BC2:} \quad \lim_{\mathbf{R}\to\infty} \mathbf{Q} = \lim_{\mathbf{R}\to\infty} \nabla\Phi = \mathbf{Q}_\infty$$

Notice that in lifting line methods the boundary conditions may be defined differently. For example by defining the downwash.

The general solution

The velocity potential can be written as the sum of a constant farfield potential (Φ_∞) plus a perturbation potential (Φ_p)

$$\Phi = \Phi_\infty + \Phi_p$$
$$\Phi_\infty = Q_\infty x$$

The *general solution* of the perturbation potential is an integral of the potentials from doublets and sources, the strength of which are μ and σ respectively, distributed over the body surface and the wake

$$\Phi(X,Y,Z) = \frac{1}{4\pi}\int_{\text{body+wake}} \mu\mathbf{n}\cdot\nabla\left(\frac{1}{r}\right)dS - \frac{1}{4\pi}\int_{\text{body}} \sigma\nabla\left(\frac{1}{r}\right)dS \qquad (2.3)$$

Notice that the wake is assumed to consist of doublets only. For a derivation of this equation see e.g. Katz and Plotkin[11]. Doublets and sources are singular elements inducing potential fields which individually are solutions of (2.1). They are described in section 2.7.

2.5.1 The general solution on discrete form

Using the knowledge that the perturbation potential can be constructed by distributing sources and doublets it is also possible to construct the velocity at a given position as the sum of perturbation velocities induced by doublets and sources ($\mathbf{Q}_\mu$ and $\mathbf{Q}_\sigma$) plus $\mathbf{Q}_\infty$

$$\mathbf{Q}(X,Y,Z) = \sum_{\text{body}} \mathbf{Q}_\mu + \sum_{\text{wake}} \mathbf{Q}_\mu + \sum_{body} \mathbf{Q}_\sigma + \mathbf{Q}_\infty$$

The velocity induced by a singularity element is proportional to the strength of the element. This means that the equation can be written on the form

$$\mathbf{Q}(X,Y,Z) = \sum_{k=1}^{N} \mathbf{Q}_k \mu_k + \sum_{l=1}^{N_W} \mathbf{Q}_l \mu_l + \sum_{k=1}^{N} \mathbf{Q}_k \sigma_k + \mathbf{Q}_\infty$$

Where indices k and l represents the singularity elements of the body and wake. N and N_W are the number of structure and wake elements respectively. $\mathbf{Q}_k$ and $\mathbf{Q}_l$ is the induced velocity at point (X,Y,Z) due to *unit strength* singularity elements. Inserting this into the Neumann boundary condition (2.2) yields

$$\sum_{k=1}^{N} \mathbf{Q}_k \cdot \mathbf{n}\, \mu_k + \sum_{l=1}^{N_W} \mathbf{Q}_l \cdot \mathbf{n}\, \mu_l + \sum_{k=1}^{N} \mathbf{Q}_k \cdot \mathbf{n}\, \sigma_k = \mathbf{v} \cdot \mathbf{n} - \mathbf{Q}_\infty \cdot \mathbf{n} \tag{2.4}$$

This equation has to hold on the body boundary. The distribution of wake singularities is also important.

2.5.1.1 Remarks

Equation (2.4) forms the basis of the numerical panel method. In the form given $\mathbf{v}$ can include any motion of the body relative to the initial coordinate system, but in the following only rotation will be included. The implementation of the equation is discussed in detail in part 4. The vortex lattice method is a special case of equation (2.4). In this method the sources are omitted and a flat geometry is chosen. This means that once equation 2.4 is implemented in a panel code the vortex lattice problem can also be solved.

2.6 The Kutta Condition

The general solution (2.3) is not unique and a condition has to be imposed. This is the Kutta condition which requires that the flow leaves the trailing edge smoothly. This is physically reasonable for most flows when the relative velocity in the flapwise direction is small compared to the velocity in the chordwise direction. It can be shown that the Kutta condition can be implemented by setting the vorticity at the trailing edge equal to zero

$$\mu_{T.E.} = 0$$

2.7 Singularity Elements

The singularity elements used in this work are described in this section. The potential fields induced by the elements are all individual solutions of (2.1). For a more thorough presentation see e.g. Katz and Plotkin[11].

2.7.1 Constant Strength Vortex

A straight vortex with constant strength Γ is the basis of many numerical solutions. The velocity induced at $\mathbf{r}_0$ (see Figure 2.4) is given by the Biot-Savart law

$$\mathbf{q} = \frac{\Gamma}{4\pi} \int \frac{d\mathbf{l} \times (\mathbf{r}_0 - \mathbf{r})}{|\mathbf{r}_0 - \mathbf{r}|^3} \tag{2.5}$$

$$\Leftrightarrow \quad d\mathbf{q} = \frac{\Gamma}{4\pi} \frac{d\mathbf{l} \times (\mathbf{r}_0 - \mathbf{r})}{|\mathbf{r}_0 - \mathbf{r}|^3} \tag{2.6}$$

Where $\mathbf{r}$ describes the vortex segment of length $d\mathbf{l}$. In numerical computations the start and end points of a vortex is given ($\mathbf{r}_1$, $\mathbf{r}_2$), and a formula for the velocity induced at a given point can be found in Katz and Plotkin[11].

$$\mathbf{q} = \frac{\Gamma}{4\pi} \frac{\mathbf{r}_1 \times \mathbf{r}_2}{|\mathbf{r}_1 \times \mathbf{r}_2|^2} \mathbf{r}_0 \left(\frac{\mathbf{r}_1}{r_1} - \frac{\mathbf{r}_2}{r_2} \right)$$

Alternatively the induced velocity can be found from the view angles β_1 and $\beta 2$. They are the angles between the vortex segment and the evaluation point evaluated at $\mathbf{r}_1$ and $\mathbf{r}_2$.

$$\mathbf{q} = \frac{\Gamma}{4\pi d} (\cos \beta_1 - \cos \beta_2) \tag{2.7}$$

Where d is the perpendicular distance from the evaluation point to the vortex segment.

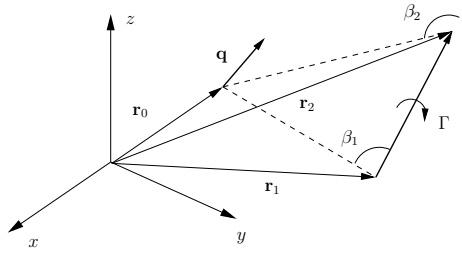

Figure 2.4: A straight vortex of constant strength Γ.

2.7.2 Constant Strength Doublet

The doublet element is equivalent to a distribution of vortices. If the strength is constant the vortices cancels everywhere except at the edges, and the element is equivalent to a vortex ring. The induced velocity can be therefore be found by combining straight vortices of the type descriped in section 2.7.1. Figure 2.5 illustrates this. Even though the element is depicted as flat it can be twisted in space and it can have any number of edges. Notice that the doublet panel has an associated vector. The induced flow is being driven through the panel in the direction of the vector and back around it.

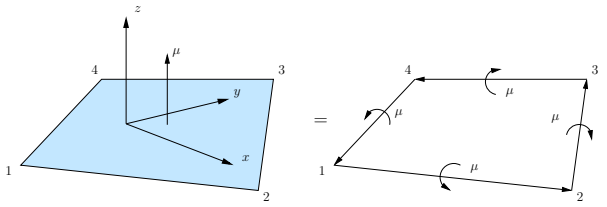

Figure 2.5: A constant strength doublet element and its vortex ring equivalent.

2.7.3 Constant Strength Source Panel

The potential induced at (x, y, z) by a constant strength source panel of strength σ positioned in the x-y plane is

$$\Phi(x,y,z) = \frac{-\sigma}{4\pi} \int_S \frac{dS}{\sqrt{(x-x_0)^2 + (y-y_0)^2 + z^2}} \tag{2.8}$$

The solution in closed form for a 3 node panel (Figure 2.6) is given in appendix A.1. The flow induced by the panel is everywhere directed away from it.

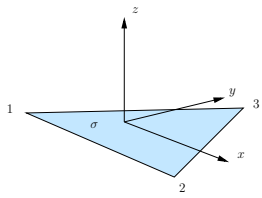

Figure 2.6: A 3 node sourcepanel.

2.8 Kutta-Joukowsky and Helmholz Theorems

The *Kutta-Joukowsky theorem* states that the force on a constant strength directed vortex element subjected to a relative velocity of $\mathbf{Q}$ is

$$\mathbf{F} = \rho\, \mathbf{Q} \times \mathbf{\Gamma} \tag{2.9}$$

The *Helmholz theorem* states that the strength of a vortex line is constant along its length, and it must form a closed loop or extend to infinity.

2.9 Wake Strength

The wake consists of doublet panels which are equivalent to trailing and shed vortex lines. The trailing lines are parallel to the flow and the shed lines are parallel to the trailing edge before they are convected downstream.

In the panel and vortex lattice methods the Kutta condition is imposed and this indirectly determines the strength of the trailing vortices. In order to set the vorticity at the trailing edge equal to zero it is necessary to attach doublet panels which cancels the vorticity and this dictates the strengths of the panels. In the following, since constant strength doublet panels are used and there is no time dependency the shed vortices corresponding to the panel edges will cancel themselves everywhere, and the wake effectively consists of vortices trailing downstream. This is the same as attaching a horseshoe vortex to the trailing edge, with the same strength as the trailing edge vorticity.

In the lifting line method the shed vortices cancels by the same argumentation as above. The strength of the trailing vortices are determined using the Helmholz theorem. Since the circulation can not end abruptly any change in circulation along the lifting line must be convected downstream in the wake. I.e.

$$\Gamma_W(s) = \frac{d\Gamma}{ds} \tag{2.10}$$

Notice that the sign will depend on the defined positive direction of the trailing wake vortices.

2.10 Wake Shape

The wake is considered to be force free. The Kutta-Joukowski theorem states that if the force on a wake vortex line is zero then

$$\mathbf{Q} \times \mathbf{\Gamma}_W = 0$$

I.e. that the velocity is parallel to the circulation vector everywhere in the wake

$$\mathbf{Q} || \mathbf{\Gamma}_W$$

2.11 The Unsteady Bernoulli Equation

If the flow is time dependent the unsteady Bernoulli Equation 2.11 must be used for pressure calculations in a panel code.

$$\left[gz + \frac{p}{\rho} + \frac{q^2}{2} + \frac{\partial \Phi}{\partial t} \right] = \left[gz + \frac{p}{\rho} + \frac{q^2}{2} + \frac{\partial \Phi}{\partial t} \right] \Bigg|_{\infty} \tag{2.11}$$

In the following the effect of gravity will be neglected. The equation will be used in the inertial (X,Y,Z) system where the flow far away is homogenious so that $\Phi|_{\infty}$=const and the time dependent term is zero. The equation is rewritten as

$$\frac{p - p_{\infty}}{\frac{1}{2}\rho} = q_{\infty}^2 - q^2 - 2\frac{\partial \Phi}{\partial t}$$

The kinematic velocity is defined as the undisturbed velocity relative to the blade

$$\mathbf{Q}_{kin} = \mathbf{Q}_{\infty} - \mathbf{\Omega} \times \mathbf{r} \tag{2.12}$$

The pressure coefficient is defined using the kinematic velocity as reference. I.e.

$$q_{ref}(\mathbf{r}) = ||\mathbf{Q}_{\infty} - \mathbf{\Omega} \times \mathbf{r}||$$

And the pressure coefficient is

$$\frac{p - p_{\infty}}{\frac{1}{2}\rho \left|\left|\mathbf{Q}_{\infty} - \mathbf{\Omega} \times \mathbf{r}\right|\right|^2} = \frac{1}{\left|\left|\mathbf{Q}_{\infty} - \mathbf{\Omega} \times \mathbf{r}\right|\right|^2} \left(q_{\infty}^2 - q^2 - 2\frac{\partial \Phi}{\partial t} \right) = C_p$$

This definition makes the pressure coefficients comparable over the span of the wing even though the pressures may vary significantly. If $\mathbf{\Omega}$=**0** the expression reduces to the standard definition of the pressure coefficient.

The term $\frac{\partial \Phi}{\partial t}$ can be evaluated in different ways. The method described here is based on a turbine rotating steadily in a plane perpendicular to the onset flow which is homogenious. I.e. no wind shear, coning angle, tilt angle and no change in time of pitch, rotational speed, windspeed etc. Except that no wind shear is allowed this approximates the working conditions of a wind turbine. Under these conditions the flowfield seen from the *rotating* body coordinate system is steady in time and therefore is

$$\frac{\partial \Phi}{\partial t}_{\text{body}} = 0$$

The relation between the time derivative in the inertial system and in the body coordinate systems is derived in [11] page 372

$$\begin{aligned} \frac{\partial}{\partial t}_{\text{inertial}} &= -\mathbf{\Omega} \times \mathbf{r} \cdot \left(\frac{\partial}{\partial x}, \frac{\partial}{\partial y}, \frac{\partial}{\partial z} \right) + \frac{\partial}{\partial t}_{body} \\ \Rightarrow \frac{\partial \Phi}{\partial t}_{\text{inertial}} &= -\mathbf{\Omega} \times \mathbf{r} \cdot \left(\frac{\partial \Phi}{\partial x}, \frac{\partial \Phi}{\partial y}, \frac{\partial \Phi}{\partial z} \right) + \frac{\partial \Phi}{\partial t}_{body} \end{aligned}$$

The space derivatives are in the body-fixed coordinate system and are therefore the velocity components in the instantaneous directions of the coordinate vectors of the rotating system

$$\frac{\partial \Phi}{\partial t}_{\text{inertial}} = -\mathbf{\Omega} \times \mathbf{r} \cdot (u, v, w)|_{body}$$

The $(u, v, w)|_{body}$ term is *not* the velocity relative to the rotating system, which is different from the velocity in the inertial system, but is simply the velocity evaluated in the inertial system divided into components in the instantaneous directions of the rotating system.

Part 3

Numerical Lifting Line Model

The lifting line model is a classical model that has been used for calculating properties of airplanes, propellers and also, to limited extent, windturbines. The basic idea is to represent all properties on a line along the span, meaning that only the overall shape of the wing is represented geometrically. The force system on the blade is described by the velocities relative to the blade and the bound circulation.

Basic properties of winglets are deduced but the principles of the method will also be used in part 4 and part 5.

3.1 Description

A numerical lifting line method capable of solving flows over wings of arbitrary shape is presented here. The wing is required to have a large aspect ratio so that the chordwise distribution of singularities on the wing can be neglected. The aspect ratio, AR, is defined as the ratio of the span to the planform area.

The mathematical solution is build from horseshoe vortex elements extending to infinity. The horseshoe vortex consists of three straight vortices with constant

and equal strength. Two of the vortices extends to infinity and the horseshoe vortex is therefore in accordance with the Helmholz theorem. In numerical applications it is enough to let the tail extend a distance far downstream. Figure 3.2.a shows the configuration. The two tails on the horseshoe vortices represents the wake and the centerpiece represents the bound circulation on the wing. Because the wake is parallel to the incoming flow it is force free. The bound circulation is perpendicular to the incoming flow and is therefore subject to a lift force. The downwash is induced by the wake and is perpendicular to both the wing and the incoming flow. This component is responsible for the induced drag.

The wing lifting line is discretized into collocation points and vortex points. The collocation points are the points of evaluation of velocities. The vortex points are the start and end points of the bound circulation vortex elements, and the positions from which the wake vortex lines are attached. The collocation points and vortex points are indicated with black and red dots respectfully, as seen in figure 3.1.

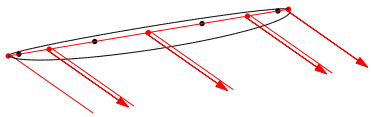

Figure 3.1: A wing and wake system represented by horseshoe vortices.

The collocation and vortex points are distributed according to a cosine spacing scheme. It will be shown that this ensures a fast convergence of the solution. The formula used to discretize a coordinate, s, in the range $s \in [a, b]$ is

$$s_i = a + \frac{\cos(x_{t1}) - \cos(x_i)}{\cos(x_{t1}) - \cos(\pi - x_{t2})} \cdot (b - a) \tag{3.1}$$

Where x is a linearly varying variable in the range $x \in [0 + x_{t1}\,, \pi - x_{t2}]$. x_{t1} and x_{t2} are truncation values that can be used to alter the shape of the distribution. They must be chosen so that x are increasing.

Flow properties are evaluated in the n_c collocation points. Since there are n_c unknowns, i.e. the strengths of the horseshoe vortices, n_c equations must be defined in the collocation points. The imposed condition is Munks theorem 2 (see Cone[2]). It states that the induced drag will be a minimum when the component of induced velocity in the direction normal to the wing (i.e. the

normalwash w_N), is proportional to the cosine of the angle of inclination, γ

$$w_N = \mathbf{Q}_i \cdot \mathbf{n} = \frac{w_0}{2} \cos(\gamma) \tag{3.2}$$

Where $\mathbf{Q}_i$ is the wake induced velocity and $\mathbf{n}$ is a normal vector. Figure 3.2 illustrates this. The blue arrows indicates the induced velocity components normal to the wing plane according to Munks theorem 2. The magnitude of w_0 is proportional to the wing loading and is not important in this context because only geometrical properties, which are independent of the loading, will be studied.

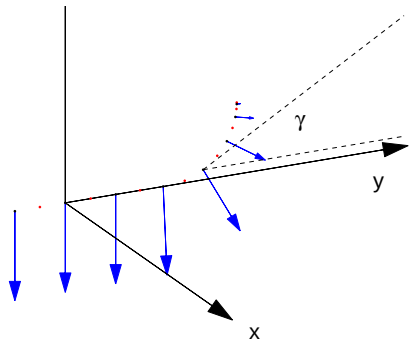

Figure 3.2: The defined optimum normal-downwash distribution

Since the induced velocity of a vortex line is proportional to the strength off it the total wake induced velocity in a given point can be written as

$$\mathbf{Q}_W = \sum_{l}^{N_W} \mathbf{Q}_l \Gamma_l$$

Where $\mathbf{Q}_l$ is the velocity induced by wake vortex l with *unit* strength. Combining this with (3.2) yields an equation that must hold in every collocation point.

$$\sum_{l}^{N_W} \mathbf{Q}_l \cdot \mathbf{n}\, \Gamma_l = \frac{w_0}{2} \cos(\gamma(s))$$

Writing this equation in all collocation points forms a linear system of equations with the strengths as the unknowns. $\mathbf{Q}_l$ can be evaluated using the formulas given in section 2.7.1.

The method will be validated against analytical results presented in section 3.2.

Remarks

The forces evaluated using the described method includes the force perpendicular to the local wing plane due to the incoming flow, and the induced drag due to velocity components induced by the wake. There is a third velocity component, the self induced velocity, which is induced by the lifting line onto itself. This force can not simply be evaluated by the Kutta Joukowsky theorem, and will be omitted in the following.

3.2 Classic Analytical Lifting Line Results

The simple geometry of airplane wings allows for an analytical treatment if the wake can be represented in a simple form as well. The plane, straight wing with a wake trailing downstream is a classical case for which analytical results exists.

An elliptic lift distribution is obtained if the planform itself is elliptic. I.e. if the chord is elliptic

$$c(y) = C_0\sqrt{1-\left(\frac{y}{b/2}\right)^2} \quad \Leftrightarrow \quad \Gamma(y) = \Gamma_0\sqrt{1-\left(\frac{y}{b/2}\right)^2}$$

Γ_0 is the circulation at the center of the wing. The downwash over an elliptic wing is constant and equal to

$$w_i = -\frac{\Gamma_0}{2bQ_\infty} \tag{3.3}$$

It can be shown that a wing with an elliptic lift distribution has the lowest induced drag of all flat wings. This is expressed in the following formula which also defines the efficiency factor k

$$C_D = \frac{C_L^2}{\pi ARk} \quad \text{, elliptic wing: } k{=}1 \tag{3.4}$$

For all plane wings k is less or equal to unity. This formula holds for non planar wings as well but k can then take values large than unity. The equation is derived in Cone[2]. Note that the aspect ratio is based on the projected area and span of the wing. k is a dimensionless parameter describing the effect of the geometry on the induced drag. It does not include any effect of viscous drag forces.

3.3 Validation

A flat wing of span b will be used as a test case to validate the numerical lifting line code. Q_∞=1 m/s. Since the wing is flat γ=0 everywhere and the optimal normal downwash according to (3.2) is constant and in the negative z-direction. This corresponds to an elliptic wing with an elliptic circulation distribution. The magnitude of the downwash is selected as $W_0/2$=1 m/s. According to (3.3) the maximum circulation is max(Γ_0)=4 m^2/s. Figure 3.3.b shows the calculated elliptical circulation distribution. The relative error of the maximum value is -0.0168% of the exact value of Γ_0=4 m^2/s. Figure 3.3.a shows the calculated efficiency factor, k, against an increasing number of collocation points, n_c. The exact analytical result is k=1 and the relative error of the numerical result is -0.0252% for n_c = 80.

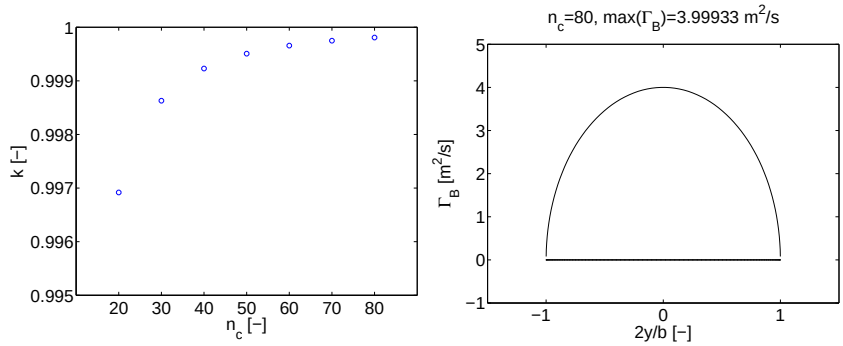

(a) Convergence with increasing spanwise discretization.

(b) The circulation distribution with n_c=80.

Figure 3.3: Validation results.

It is concluded that the numerical lifting line is accurate and that a relatively coarse discretization is sufficient. In the test example above a cosine spacing was used with success. Calculations has been made on a wing with rounded winglets attached. The winglet height is h=0.2 b and the curve radius is R=h. Figure 3.4.a compares the computed k-values using the linear and cosine discretization respectively. The values converges very fast to k=1.2527 when the cosine spacing is used. Further tests shows that 2000 collocation points are needed for the results of the linear spacing to converge to k=1.2530.

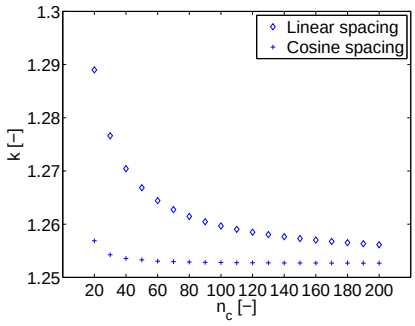

Figure 3.4: Convergence of k for a wing with rounded tips using cosine and linear spacing.

3.4 Effect of Winglet Height and Curve Radius

A parameter study is made for a wing with vertical winglets attached to the suction side. The corner is rounded with varying curve radius. This shape is believed to represent important geometrical properties. The following quantities has been varied in the study

$\frac{R}{h}$ The ratio of curve radius to winglet height. A value of 1 is equivalent to a completely rounded tip. $\frac{R}{h} \in [0.25, 0.95]$.

$\frac{b}{h}$ The ratio of wingspan to winglet height. Large values means small winglets. $\frac{b}{h} \in [5, 75]$.

Figure 3.5 shows the results. The value of k is highest for relatively large winglets. The effect of curve radius is not as significant but is important for small values of $\frac{b}{h}$. In general, the smaller curve radius the better, but in a viscous flow there is an increased risk of separation in a corner and the best compromise is to round the corner.

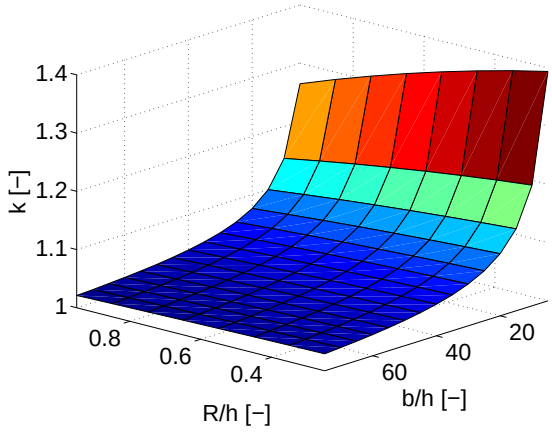

Figure 3.5: Results of parameter study.

3.5 Optimum Circulation distribution on Wings

Calculations has been made on a wing with 5% winglets (h/b=0.05) and varying curve radius. The bound and wake circulation strength will be studied. The bound circulation is the solution from the numerical lifting line code. The wake strength is found as

$$\Gamma_W = -\frac{d\Gamma_b}{ds}$$

Where s is a surface parameter along the span. Note that the wake strength found in this way is not the strength of the discretized horseshoe vortices but is instead the distributed strength or strength per length.

Figures 3.6, 3.7 and 3.8 shows the results and the contours of the wing. The wake strength, Γ_W, increases locally in the bend, and especially for small curve radius the increase is large. This is caused by the bound circulation distribution, Γ_B, having a larger derivative locally in the bend. In all cases the wake strength has a maximum at the winglet tip and this indicates that the bound circulation distribution should also have a large derivative near the winglet tip. Except for local changes in the bend it appears that the optimum bound circulation can be found by simply extending the elliptic circulation distribution over the winglet. Winglets with a sharp bend is clearly more effective than rounded winglets. In this case k=1.056 for R_c/h=0% and k=1.043 for R_c/h=80%.

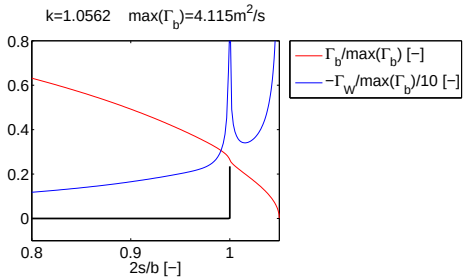

Figure 3.6: Circulation distribution over wing with 5% winglet and 0% curve radius.

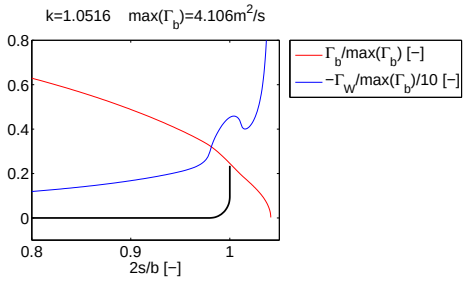

Figure 3.7: Circulation distribution over wing with 5% winglet and 40% curve radius.

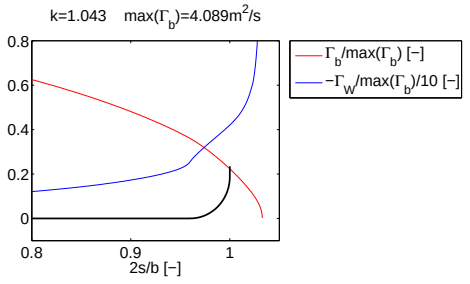

Figure 3.8: Circulation distribution over wing with 5% winglet and 80% curve radius.

3.6 Generalization of Wing Results to Turbines

Some of the results found in this part can be generalized to turbines. Based on the discussion and results of part 5 the winglet acts locally and has no effect on the wake except for immediately behind the trailing edge. It is therefore expected that physical properties of turbine winglets resembles those of wing mounted winglets.

The circulation distribution over well designed turbine blades differs substantially from the elliptic distribution over wings. Turbine blades tends to have a constant circulation over the center part but near the tip the shape approximates that of wings. Therefore it can be expected that the circulation on well designed winglets should be distributed somewhat similar to what was found in section 3.5. This is important from a design point of view and will be used in part 5 to define the circulation on the outer part of the blade. Note that a theorem similar to Munks theorem 2, to this authors knowledge, does not exist for turbines and an optimum distribution of circulation can not be calculated directly.

Winglets are found to be most effective if the bend is sharp with a small rounding radius. This is believed to be true for turbines as well.

3.7 Force and Viscous Drag Calculation Using Lifting Line Data

In the previous sections only the geometrical properties relatated to the induced drag was investigated. The viscous drag is several times larger than the induced drag and will be included in the calculations henceforth. A method for calculation of the viscous force on a lifting line is described below. The inviscous force on a bound vortex of finite length is calculated using the Kutta Joukowsky theorem (2.9). To get the section force, $f(s)$, divide the force by the length of the vortex [1]

$$\mathbf{f}(s) = \frac{\rho\,\mathbf{Q} \times \mathbf{\Gamma}}{||\mathbf{\Gamma}||}$$

The total force and moment is found by integration over the lifting line

$$\mathbf{F}_j = \int \mathbf{f}(s) ds \tag{3.5}$$

[1] The bound vorticity is assumed to be discretized into constant strength vectors, $\mathbf{\Gamma}$

$$\mathbf{M}_j = \int \mathbf{r}(s) \times \mathbf{f}(s) ds \tag{3.6}$$

The 3D numerical, inviscid methods are capable of calculating induced drag, and this component is directly included in the calculated force. The missing drag components are the pressure, or form drag, and the friction drag. Both of them can be estimated using 2D experimental data. Both drag forms are due to viscous effects, and the total drag is termed viscous drag. Since the effect of the 3 dimensional wings are effectively to change the local flow properties, care has to be taken so that the correct reference velocities are used when accessing 2D data.

A method based on lifting line data and Lift-Drag polars are presented in the following.

The viscous drag is by definition in the direction of the onset flow. In experiments the onset flow is often uniform, but here the local flow velocity $\mathbf{Q}$ must be used. The direction is

$$\mathbf{t}(\mathbf{s}) = \frac{\mathbf{Q}(\mathbf{s})}{||\mathbf{Q}(\mathbf{s})||}$$

$\mathbf{Q}$ must include all velocities. Since the theory is not linear it is in general not possible to decompose it, the exception being when a constant lift to drag ratio is assumed. The velocities induced by the wing itself represents a numerical problem and can not be evaluated in the lifting line method. The direction of these velocities are in most cases in the direction of $\mathbf{t}$, and does not affect the solution (i.e. the Γ-values), but they will have an effect on the reference velocities and should therefore be estimated and included in the viscous drag model if possible. As an approximation, if the winglets are small, they can be neglected and will be in this work. The section force, $f(s)$, is used to calculate the section lift coefficient, C_l. Notice that this local force is rotated by the local wing angle, γ, and the induced angle of attack. $f(s)$ is assumed to be known along the lifting line. The reference velocity in the definition of C_l is the local flow velocity.

$$q_{ref} = ||\mathbf{Q}(\mathbf{s})||$$

The section lift coefficient is

$$C_l(s) = \frac{f(s)}{1/2 \rho q_{ref}^2 c(s)}$$

Using 2D table look up the section drag coefficient is found as a function of C_l

$$C_d(s) = C_d\left(C_l(s)\right)$$

The viscous section drag, $d(s)$, is then determined from its definition

$$C_d(s) = \frac{d(s)}{1/2\rho q_{ref}^2 c(s)}$$

Finally the total friction force and moment can be integrated

$$\mathbf{F}_v = \int d(s)\mathbf{t}(s)ds \tag{3.7}$$

$$\mathbf{M}_v = \int \mathbf{r}(\mathbf{s}) \times [d(s)\mathbf{t}(s)]\, ds \tag{3.8}$$

For turbines the total power and thrust coefficients are based on the moment about the x-axis and the x-component of the forces

$$C_p = \frac{(M_{j,x} + M_{v,x})\,\Omega}{1/2\rho Q_\infty^3 A} \tag{3.9}$$

$$C_T = \frac{F_{j,x} + F_{v,x}}{1/2\rho Q_\infty^2 A} \tag{3.10}$$

Where A is the swept area. A blade section contributes with the moment, M'_x, about the x-axis and the section power coefficient, C'_p, is defined as

$$C'_p = \frac{M'_x \Omega}{1/2\rho Q_\infty^3 A} \tag{3.11}$$

Likewise the section thrust coefficient is defined as

$$C'_T = \frac{F'_x \Omega}{1/2\rho Q_\infty^2 A} \tag{3.12}$$

The section power and thrust coefficient are dimensionless torque and force values which will be used for presentation of results.

Validation

The method is validated against work of Gaunaa et al.[5]. They present the C_p-value at a tip speed ratio of λ=8 calculated using a free wake lifting line method (FWLL) and CFD on the corresponding 3 dimensional geometry. The induced velocities and the circulation distribution along the blade are used as input and can be found in section 4.5.

A constant lift to drag ratio of 110 is used (i.e. $C_d = C_l/110$). In table 3.1 the reported results are compared to equation (3.9) and (3.10). The C_p and C_T value is 0.4% and 0.7% less than the reported CFD result. Based on this relative good agreement the method is considered validated. The error on the thrust is to large to be acceptable but since the major concern in the following is the power production it will be accepted. There is a possibility that the disagreement is because of the differences in flow properties predicted by the various models.

	C_p	C_T
CFD, Gaunaa et al.[5]	0.515	0.872
FWLL, Gaunaa et al.[5]	0.514	0.868
(3.9) using FWLL data, (3.10)	0.513	0.866

Table 3.1: Validation of (3.9) and (3.10).

3.8 Conclusions

In this part preliminary results for winglets are found. The lifting line representation of data will be used in the following parts for calculation of forces and as the basis of the design method. The bound circulation distribution over optimal loaded wings was found and will be used in the design algorithm.

Part 4

A Freewake, Vortex Lattice and Panel Method

The lifting line method presented in part 3 can be used very successfully for high aspect ratio wings but lacks the ability to accurately model wings of low aspect ratio. Even though modern turbine blades are very slender, they do have significant chord lengths close to the hub, where the lifting line representation can not be considered accurate. The vortex lattice method and the panel method both includes the effect of the chordwise distribution of properties and the methods are presented in the following.

It turns out that both the vortex lattice and the panel method has severe shortcomings when simulating the forces on rotating turbines. Mainly, the degree of accuracy when evaluating forces, and the fact that a turbine is almost certain to stall over a smaller or larger part of the blade near the hub, making the inviscid flow assumption invalid, has a pronounced effect on the accuracy. The accuracy can be improved by using higher order methods, but this is hardly worth the effort since there is still a number of issues regarding the validity of using potential flow for simulation of windturbines. Today it is possible to make a full CFD calculation in 24 hours and this makes it a more appealing alternative to use simple fast models for initial design and CFD calculations for validation and final designs.

The method presented is based on constant strength doublet and source panels

and is termed a first order method. Higher order methods uses varying strength panels. The implemented code can be used as both a panel and a vortex lattice method.

4.0.1 Description

Equation (2.4) repeated below states the condition of zero normal flow on the body surface and forms the basis of a numerical solution

$$\sum_{k=1}^{N} \mathbf{Q}_k \cdot \mathbf{n}\, \mu_k + \sum_{l=1}^{N_W} \mathbf{Q}_l \cdot \mathbf{n}\, \mu_l + \sum_{k=1}^{N} \mathbf{Q}_k \cdot \mathbf{n}\, \sigma_k = \mathbf{v} \cdot \mathbf{n} - \mathbf{Q}_\infty \cdot \mathbf{n} \tag{4.1}$$

To implement it it is nescessery to define the blade and wake singularities. First consider the N blade source and doublet elements. The blade is described by nodes that are formed into panels consisting of 4 nodes each. The panels can be twisted in space which means that any geometry can be represented, as opposed to using flat panels only. A collocation point is placed at the center of each panel and it has an associated normal vector pointing away from the structure. The constant strength doublet panel (section 2.7) is defined based on the 4 corner points of a panel. This is illustrated in Figure 4.1 along with the collocation point and normal vector.

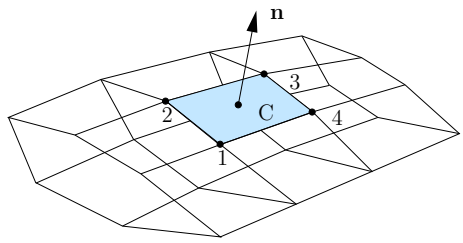

Figure 4.1: A constant strength doublet panel.

A 3 node source-panel has been implemented in order to be able to describe the twisted source panel and the panel is split into 4 panels with a common center node. The center node is placed a small distance below the collocation point. This is important since if the collocation point had been below the panel it would appear in the equations that the panel is creating suction instead of blowing. The constant strength doublet panel is equivalent to a vortex ring, and therefore is the exact placement of the collocation point relative to it not important, as long as it is approximately at the center.

N collocation points is now defined on the body surface which consists of N panels. Since each panel has associated both a μ and a σ value the number of unknowns are twice the number of available linear equations. Therefore, the source strengths can be defined and only the doublet strengths are solved for. In the Neumann formulation of the problem used here, the strengths can be choosen freely. However they should be choosen wisely in order to avoid numerical problems. The source strengths are set equal to the negative of the magnitude of the normal flow due to freestream and structural velocities

$$\sigma = -\mathbf{n} \cdot (\mathbf{Q}_\infty - \mathbf{v})$$

Directly above a panel the velocity induced by it, is

$$\begin{aligned} \mathbf{Q}_i &= \frac{1}{2}\sigma \mathbf{n} \\ \Rightarrow \mathbf{Q}_i &= -\frac{1}{2}(\mathbf{n} \cdot (\mathbf{Q}_\infty - \mathbf{v})) \cdot \mathbf{n} \end{aligned}$$

Therefore, $\mathbf{Q}$ is exactly half the normal flow due to $(\mathbf{Q}_\infty - \mathbf{v})$ and in the opposite direction. This choice is made because it makes the solution numerically stable. Evaluating the terms related to body singularities in the N collocation yields a linear system of equation which can be put on matrix form

$$\begin{bmatrix} \vdots \\ \sum_{k=1}^{N} \mathbf{Q}_k \cdot \mathbf{n}\, \mu_k + \sum_{k=1}^{N} \mathbf{Q}_k \cdot \mathbf{n}\, \sigma_k \\ \vdots \end{bmatrix} = \mathbf{A}_\mu \mu + \mathbf{A}_\sigma \sigma \tag{4.2}$$

Where μ and σ are vectors of the panel doublet and source strengths.

The wake is modeled as a distribution of constant strength doublet panels. Since only steady state solutions will be considered (i.e. no change in time of the bound circulation) the doublet panels trailing of the same spanwise position will have the same strength and the circulation at the edges they have in common cancels everywhere. The wake is therefore equivalent to horseshoe vortices attached to the trailing edge. The strengths of the horseshoe vortices are defined by the Kutta condition which states that the circulation at the trailing edge must cancel. In order to do so the wake horseshoe vortex must have a strength that depends on the trailing edge doublet strengths

$$\mu_l = \mu_{k1} - \mu_{k2}$$

This is illustrated in Figure 4.2 which shows two adjoining panels at the trailing edge and an attached horseshoe wake element extending downstream.

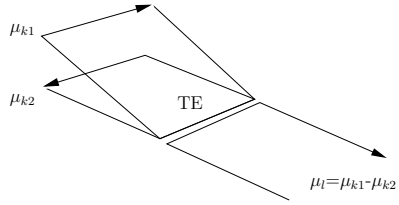

Figure 4.2: A horseshoe vortex attached to the trailing edge.

In (4.1) the influence of the wake is included in the term

$$\sum_{l=1}^{N_W} \mathbf{Q}_l \cdot \mathbf{n}\mu_l$$

The contribution from a horseshoe vortex to the sum is

$$\sum_{l=1}^{N_W} \mathbf{Q}_l \cdot \mathbf{n}\mu_l(\mu_k) = \cdots + \mathbf{Q}_l \cdot \mathbf{n}(\mu_{k1} - \mu_{k2}) + \ldots$$

And therefore will the wake influence effectively depend on the strength of the blade doublet panels at the trailing edge. If a flat vortex lattice geometry is used the wake strength will only depend on the strength of one panel. In practice the wake consists of a large number of vortices and only the ones directly attached to the trailing edge depends on the trailing edge doublet strengths. The downstream vortices have an absolute fixed strength. This change in wake strength downstream is caused by the initial developing flow of a time marching scheme. In the developing phase the horseshoe representation is not valid, but this part of the wake is quickly convected away from the blade and is eventually cut away. The total influence of the wake is split into the N_{TE} dependent vortices at the trailing edge and the remaining constant strength vortices far downstream

$$\sum_{l=1}^{N_W} \mathbf{Q}_l \cdot \mathbf{n}\mu_l = \sum_{l=1}^{N_{TE}} \mathbf{Q}_l \cdot \mathbf{n}\mu_l(\mu_k) + \sum_{l=1+N_{TE}}^{N_W} \mathbf{Q}_l \cdot \mathbf{n}\mu_l$$

Evaluating this term in the N collocation points yields a linear system

$$\begin{bmatrix} \vdots \\ \sum_{l=1}^{N_{TE}} \mathbf{Q}_l \cdot \mathbf{n}\mu_l(\mu_k) + \sum_{l=1+N_{TE}}^{N_W} \mathbf{Q}_l \cdot \mathbf{n}\mu_l \\ \vdots \end{bmatrix} = \mathbf{A}_W\mu + \mathbf{A}_{W2}\mu_W \qquad (4.3)$$

Where μ_W is a vector with the strengths of the downstream independent wake vortices. The shape of the wake has a significant impact on the solution and

care must be taken in order to determine it. This is especially important when calculating the flow past wind turbines, but for wings in steady forward fligth good results can be obtained simply by letting the wake trail downstream. The calculation of the wake shape behind wind turbines is discussed in section 4.1.

Combining (4.1), (4.2) and (4.3) yields

$$(\mathbf{A}_W + \mathbf{A}_\mu)\mu + \mathbf{A}_{W2}\mu_W + \mathbf{A}_\sigma\sigma = \mathbf{a}$$

Where $\mathbf{a}$ is the vector of $\mathbf{v} \cdot \mathbf{n}$-$\mathbf{Q}_\infty \cdot \mathbf{n}$ evaluated in the collocation points. This is rearranged as

$$\begin{aligned}(\mathbf{A}_W + \mathbf{A}_\mu)\mu &= \mathbf{a} - \mathbf{A}_{W2}\mu_W - \mathbf{A}_\sigma\sigma \\ \mathbf{A}\mu &= \mathbf{b}\end{aligned}$$

This system can now be solved for the unknown doublet distribution.

Notice that $\mathbf{A}_\mu$ and $\mathbf{A}_\sigma$ are constant when there is no deformation of the structure (rotation is allowed). If Ω and $\mathbf{Q}_\infty$ is also constant then so is $\mathbf{a}$. When stepping in time it is therefore only necessery to update $\mathbf{A}_W$, $\mathbf{A}_{W2}$ and μ_W before solving the equations. A flowchart for the algorithm is seen in Figure 4.3.

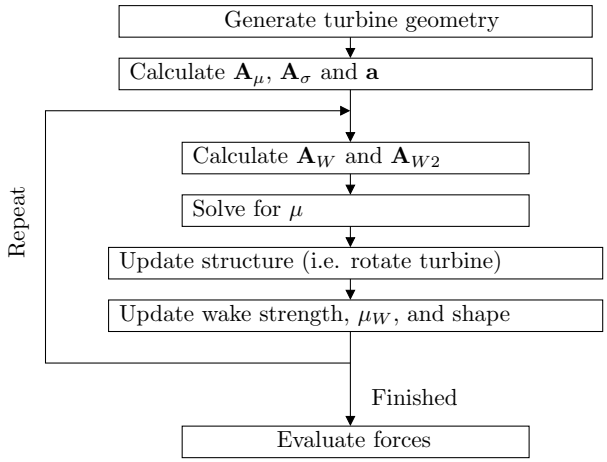

Figure 4.3: Flowchart for solving (4.1).

4.1 Freewake Model

The free wake is generated by letting vortices trail of the blade as the turbine rotates, and then convect the vortices downstream according to an Euler time

marching scheme. For each time step the position of the vortex nodes are updated as

$$\Delta \mathbf{X} = \mathbf{Q} \Delta t$$

Where $\mathbf{Q}$ is the total velocity, but not including velocities induced by the vortex itself. This is the basic idea but it does not work very well without some modifications. The problems are related to stability, excessive computational time, and that the shape of a fully developed wake is needed. The total simulation time is set according to 8 revolutions of the rotor t_{total}.

To enhance speed a wake roll up procedure has been implemented. At time t_{R1} the procedure begins and at time t_{R2} the wake consists of just a tip and a root vortex. The root vortex has the strength of all the trailing vortices from the root until a position just before the center of the blade. The tip vortex has the strength of the trailing vortices from the center and out.

To enhance stability a number of improvements has been included. If a wake node is past a specified x-position, x_P, it is only moved in the x-direction according to the u-velocity component. Thereby it is assumed that the wake has reached its maximum expansion. The initial wake shape is not correct and at simulation time t_C all vortices older than a specified age, $t_{C,age}$, is removed. A prescribed wake of limited size is attached to the oldest vortices that otherwise would have a free end. Without it the wake becomes unstable. The strength is the same as that of the vortex to which it is attached. It has a helical shape according to an assumed downstream velocity Q_{pre}. Its downstream length is $Q_{pre}t_{pre}$. A viscous core model has been implemented. The main effect of this is to eliminate the very large velocities close to the wake vortices since this makes the wake very unstable. The viscous core model is physical correct since it models the decrease in velocity near the center of a wake vortex, and therefore the development of the wake becomes reasonable. From a mathematical point of view the viscous core model is not correct, and therefore care has been taken to ensure that it has no effect near the rotorplane, since changes in induced velocities directly affects the solution. The implemented viscous core model is described in detail in Sant[13] and the equations are given here. The Biot-Savart relation (2.6) is modified by a scaling factor, K_v

$$d\mathbf{q} = K_v \frac{\Gamma}{4\pi} \frac{d\mathbf{l} \times (\mathbf{r}_0 - \mathbf{r})}{|\mathbf{r}_0 - \mathbf{r}|^3}$$

K_v is calculated from physical properties and the vortex age, t

$$K_v = \frac{h^2}{(r_c^4 + h^4)^{1/2}}$$
$$r_c = \sqrt{4\alpha\delta_v\nu(t + S_c)} \quad \text{, t >= -}S_c$$
$$r_c = 0 \quad \text{, t <= -}S_c$$

Where h is the perpendicular distance from the vortex to the evaluation point. α is a constant equal to 1.25643. ν is the kinematic viscosity and S_c is an age offset constant. δ_v is a turbulent viscosity coefficient.

Table 4.1 summaries the parameters used in the simulation of a 30 meter turbine at a tip speed ratio of λ=8. The resulting wake is seen in Figure 4.4.

t_{R1}=6 s	t_{R2}=10 s	X_p=8 m	t_{total}=18.85 s
t_C=10	$t_{C,age}$=6	Q_{pre}=1/3 Q_∞	t_{pre}=4 s
S_c=-2.5	δ_v=100	ν=1.51e-5	

Table 4.1: Freewake simulation parameters used in simulation of 30m rotor. λ=8. Q_∞=10 m/s .

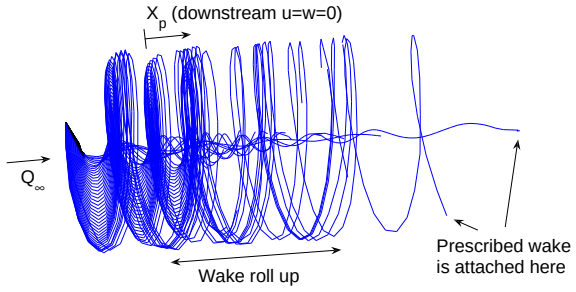

Figure 4.4: The developed wake.

4.2 Evaluation of Forces

The method for evaluation of forces depends on whether the panel or vortex lattice method is used. A third method that can be applied to both of the above mentioned, is to transfer data to a lifting line and then evaluate the forces. The methods are described in the following.

4.2.1 Panel Method

In the panel method the pressures on the collocation points can be calculated using the unsteady Bernoulli equation (2.11). The force on panel i of area A_i is

$$\mathbf{F}_i = -p_i \cdot \mathbf{n}\, A_i$$

The minus sign reflects that a positive pressure acts against the outward pointing normal vector.

When using the Bernoulli equation it is nescessery to evaluate the velocities induced by the doublet panels onto themself in a special way. The reason is that the constant strength doublet panel mainly induces a velocity onto itself in the normal direction and the tangential velocities on the collocation points are therefore to small. This has only a small effect on the solution (i.e. the doublet distribution) since it is based on the zero normal flow condition, but it has a large effect on the pressure distribution. The solution is to assume a more realistic distributed doublet distribution instead of the piecewise constant distribution. The induced tangential velocities can then be evaluated using analytical formulas for the induced tangential velocities on doublet panels. If l and m are chordwise and spanwise surface parameters, then the induced velocities in the respective directions are

$$q_l = -\frac{\partial \mu}{\partial l} \quad q_m = -\frac{\partial \mu}{\partial m}$$

4.2.2 Vortex Lattice Method

In the vortex lattice method the forces are obtained by applying the Kutta-Joukowsky theorem on each bound vortex. The velocity used is the total velocity

$$\mathbf{F}_i = \rho \mathbf{Q_i} \times \mathbf{\Gamma_i}$$

The best result is obtained if the velocities are evaluated in the collocation points and then interpolated onto the bound vortices using appropriate surface parameters. When this method is used an important force component, the leading edge suction, is missing. Since this has a large influence on the power production of turbines it was decided to use the method described next.

4.2.3 Lifting Line

The forces evaluated on a lifting line includes the leading edge suction, but any forces due to velocities induced by the structure onto itself can not be evaluated.

This is not a serious problem since these forces are relatively small and confined to the tip area. The major part of this force will be lift, and omitting it gives a conservative estimate on the power production and the thrust. The evaluation of forces on the lifting line is described in section 3.7.

To obtain the lifting line circulation distribution the strength of spanwise bound vortices are summed over the chord at all spanwise positions. The spanwise bound vortices are the vortices in the vortex lattice grid which are aligned with the spanwise direction. The lifting line velocity is more subtle. The induced velocity is induced by both the wake and the bound vortices, but in the lifting line representation the velocities induced by the bound vortices must be omitted. Since the wake induced velocities has large variations over the chord, it is not clear which value to use. A solution is to recalculate the wake induced velocities on the lifting line by extending the wake so it is attached directly to the lifting line instead of the trailing edge of the 3 dimensional blade.

Table 4.2 compares calculated results for a flat AR=10, b=10 elliptic flat wing in homogenious flow. The lift coefficients are very similar but the induced drag coefficient calculated in the vortex lattice code, as described in section 4.2.2, is to high. This is because of the missing leading edge suction. The forces evaluated by transfering the bound circulation and velocities to the lifting line agrees very well with the analytical results, and this method will be used henceforth.

	C_L	C_{Di}
Vortex Lattice	0.88289	0.15098
Liftin Line (Transfered Γ_b)	0.88223	0.024819
Analytical (Based on Γ_0=max(Γ_b))	0.88307	0.024822

Table 4.2: Comparison of methods for force evaluation.

4.3 Calculation of Wing Geometries for Vortex Lattice Simulations

A major problem with wind turbine simulations is to predict the wake influence in the rotorplane. Because of this it was eventually decided to focus on the bound circulation distribution and the wake induced velocities in the lifting line representation and not any chordwise distribution of properties. Therefore it is not necessary to design a wing that represents the exact shape of the physical wing, which will often be designed to satisfy a number of practical design issues, but instead use a geometry which is more suitable from a computational point of view. As long as the blade generates the correct circulation distribution in

the given velocity field its trailing wake will be correct and therefore also the influence of it (assuming the wake model is correct).

The blade profiles used in the Vortex Lattice simulations are selected as flat without camber because they are well defined and therefore eliminates one source of uncertainty. At a given condition a flat blade can be defined in an infinity number of ways in order to generate a given lift, since both the angle of attack and the chord can be varied, but it should be designed to generate correct results at off design conditions.

The angle of attack of any profile is a function of the lift coefficient, and is therefore dictated by the choice of it. In the linear range the relationship is

$$\begin{aligned} C_l &= a_0(\alpha + \alpha_0) \quad \text{, in general (physical blade)} \\ C_{l,f} &= 2\pi(\alpha) \quad \text{, flat blade (vortex lattice)} \end{aligned}$$

Where C_l and $C_{l,f}$ are the lift coefficients of the physical (real) blade and the blade used in simulations, respectfully. The flat plate is given an offset angle equal to α_0, because the ratio between C_l and $C_{l,f}$ is then constant and equal to $a_0/2\pi$ at all inflow angles. This is important because it guarantees the correct behavior of the flat blade at off-design conditions. In general $C_{l,f}$ will be larger than C_l since $a_0 < 2\pi$, and the chord of the flat plate (c_f) should be adjusted so that the lift generated at a given inflow angle is the same for both the physical and the flat blade. I.e.

$$\begin{aligned} C_{l,f} &= \frac{2\pi}{a_0} C_l \\ \frac{L}{1/2\rho Q^2 c_f} &= \frac{2\pi}{a_0} \frac{L}{1/2\rho Q^2 c} \\ \Rightarrow \quad c_f &= \frac{a_0}{2\pi} c \end{aligned}$$

c_f is the chord of the flat blade. Figure 4.5 shows an example of a physical profile and the vortex lattice equivalent.

Figure 4.5: A realistic blade and a flat blade suitable for Vortex Lattice calculations. Both are at defined zero degree angle of attack

4.4 Grid Generation

The panel grid has N_{upper} and N_{lower} panels on the upper and lower side of the blade. If a grid for vortex lattice simulations are created N_{upper} is zero. N_{span} is the number of spanwise stations. The importance of the grid layout is well described in the literature and will not be threated in detail here. The panels are distributed according to a cosine spacing scheme in the spanwise direction on both the upper and lower side, in order to group the panels closer together near the leading edge/trailing edge and the tip/root. Figure 4.6 shows an example of a grid layout. The grid is very coarse and in practice a finer mesh is used with the discretization parameters given in table 4.3. This discretization was selected because the results were reasonable and finer grids would lead to very large computational times. x_{ij} refers to the truncation values defined in (3.1).

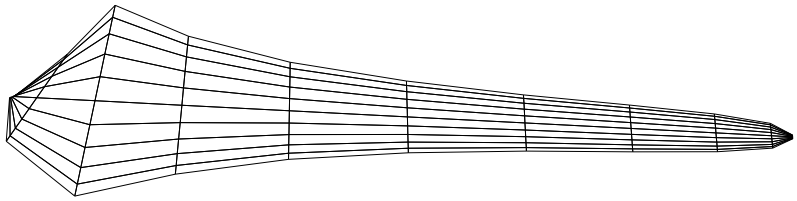

Figure 4.6: Example of a coarse vortex lattice grid.

	# panels	(root/trailing edge)	(tip/leading edge)
Vortex lattice	N_{chord}=25	x_{t1}=0.4	x_{t2}=0.4
	N_{span}=55	x_{t1}=0.05	x_{t2}=0.025

Table 4.3: Vortex lattice discretization parameters.

4.5 Reference Blade Data

The turbine blade data presented in this section is used for validation and as reference values for a flat blade. The tip speed ratio is λ=8.

The calculated power and thrust coefficients and the distributed loads has been verified against CFD calculations (see Ganuaa and Johansen[5]). Figure 4.7 shows the wake induced velocities and the bound circulation along the span. In

the following only the wake induced velocities will be stated because the other velocity components are known. I.e. the kinematic velocity, (2.12).

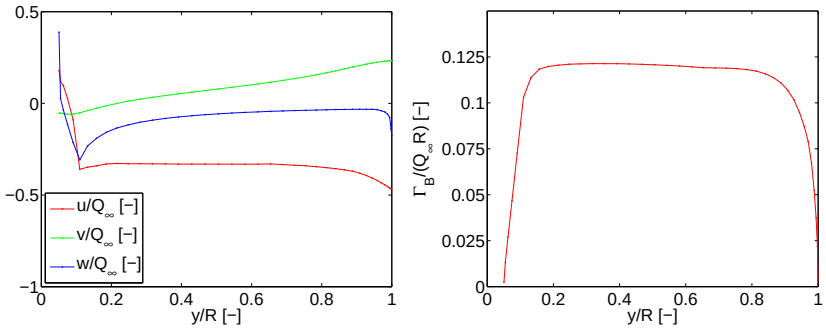

Figure 4.7: The induced velocities and bound circulation.

Figure 4.8 shows the twist and chord distribution according to the Risø-B118 profile at 8 degrees angle of attack.

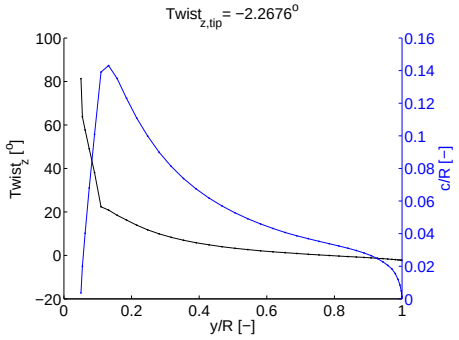

Figure 4.8: Twist and chord distribution.

The power and thrust coefficients are given in table 4.4.

C_p	C_T
0.513	0.866

Table 4.4: Power and thrust coefficient for flat reference blade.

4.6 Validation

The vortex lattice code is validated against the results for the flat blade presented in section 4.5 operating at a tip speed ratio of 8. The turbine was scaled to a radius of 30 meter, and the free wake parameters given in table 4.1 was used. The velocities and forces are found by representing data on the lifting line as described in section 3.7.

Figure 4.9 and 4.10 compares the inviscous and the viscous forces to the design goal (i.e. the input data). The inviscous forces are forces calculated using the Joukowsky theorem and viscous forces are drag forces. The agreement is relatively good but the forces are to large at center of the blade. Near the root the forces has some error but this has very little effect on C_p.

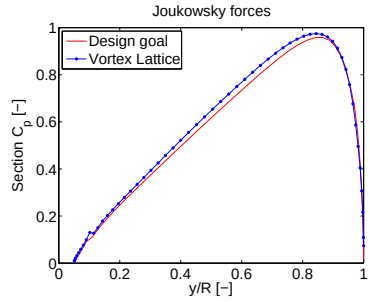

Figure 4.9: Section C_p due to the inviscous Joukowsky forces compared to design values.

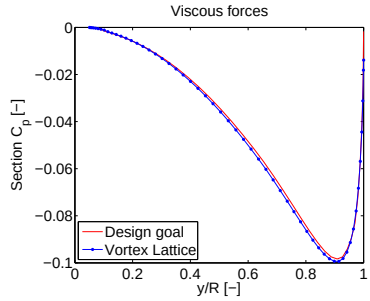

Figure 4.10: Section C_p due to Viscous forces compared to design values.

Figure 4.11 compares the bound circulation. The calculated values are to large

at the center, which explains the discrepancy found above.

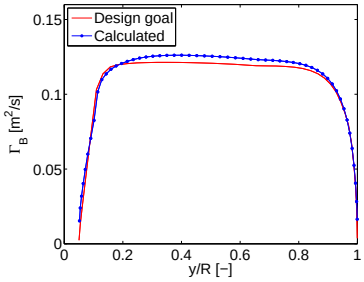

Figure 4.11: Γ_B compared to design values.

In Figure 4.12 the inflow angles are compared. There is a large error near the root, and over the center of the blade the inflow angle is to high (approximately 1/2 degree).

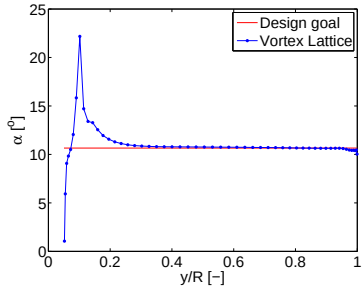

Figure 4.12: The local inflow angle compared to the design value.

The wake induced velocities are shown in figure 4.13. The data agrees reasonable well over the center of the blade but some discrepancy is found near the tip and root.

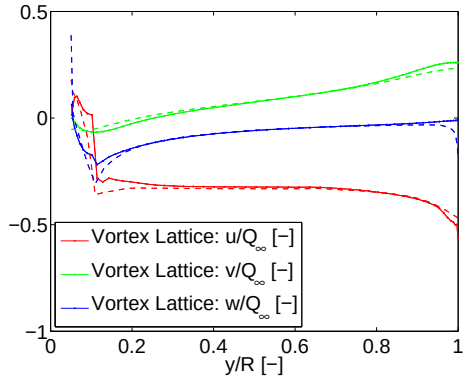

Figure 4.13: Comparison of calculated induced velocities and design values (dashed)

A summary of important data is found in table 4.5. Notice that the axial induction is to small, which explains why the force and angle of attack is to high. The error is probably in the wake model which does not accurately predict the axial induction.

	Design goal	Vortex Lattice
Axial induction, a (y/R=0.5)	0.3314	0.3233 (-2.4%)
C_p	0.513	0.531 (+3.5%)
C_T	0.866	0.887 (+2.4%)

Table 4.5: Comparison of important parameters

It is concluded that the vortex lattice code captures the physics of the flow but with an error of 3.5% on the power. It can therefore not be expected that the method can accurately predict turbine performance but it may be usefull for studying variations in flow properties.

4.6.1 Validation of Panel Code

To validate the panel code a turbine rotating with constant rotational speed is considered. The wake is completely omitted meaning that the spanwise undisturbed velocity distribution relative to the blade is known but the results are not physically correct. The wake model will not be verified since it was included in the vortex lattice calculations above. The undisturbed velocity seen

at a spanwise position is then the kinematic velocity

$$\mathbf{Q}_{kin} = \mathbf{Q}_{\infty} - \mathbf{\Omega} \times \mathbf{r}$$

Based on this a twist distribution can be calculated which corresponds to a given angle of attack.

Calculations has been made on a turbine with a chord that varies linearly from 3 m at R=3 m to 1 m at the tip, R=30 m. The symmetric Van De Vooren profile with 15% thickness and 12.^{o} trailing edge angle is used because the analytical pressure distribution is known (see Katz and Plotkin[11]). The pressure coefficients, calculated at a spanwise position of $\frac{y}{R}$=0.76 using the unsteady Bernoulli equation is shown in Figure 4.14. The agreement with the analytical result is good, considering that 3 dimensional effects can not be completely neglected.

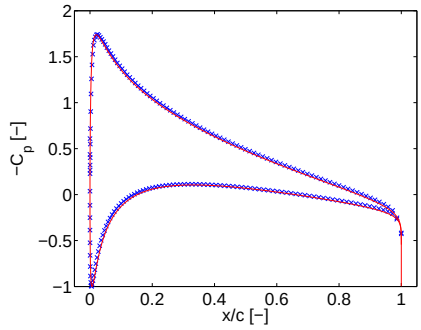

Figure 4.14: Comparison of analytical and numerically calculated pressure coefficients at spanwise position $\frac{y}{R}$=0.76 .

The panel code is accurate but the computational time is in the order of 12-24 hours. This is mainly because a very high number of panels is needed. Figure 4.15 shows lift coefficients against the number of panels on the upper and lower side for an elliptic flat wing of aspect ratio 10 at 8^o angle of attack. The wake model is included. 100 panels on the upper and lower side is not enough to ensure converged results. Figure 4.16 shows the distributed C_p values.

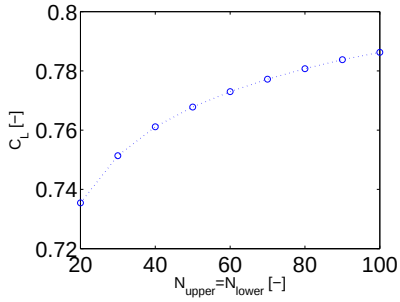

Figure 4.15: Convergence of lift coefficient against chordwise discretization.

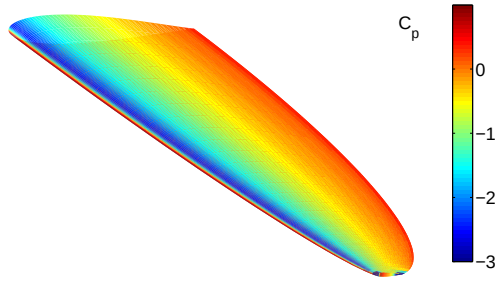

Figure 4.16: Distributed C_p values.

4.7 Conclusions

The panel and vortex lattice codes have been validated. Because of uncertainties in the free wake model and the use of relatively coarse discretization due to excessive computational time, the accuracy is limited to within ≈3-5%. This is relatively accurate but the uncertainty is larger than the expected increase in C_p, and it is questionable whether the effects of wingles can be predicted using the methods described in this part.

Part 5

Blade and Winglet Design

This part issues the design of winglets. Vortex lattice simulations of a poor design are not interesting and the need for a design algorithm is apparent. A method will be developed which is found to be fast and numerically consistent.

The method is based on input in the form of a known bound circulation and velocity distribution of a flat blade. The input velocity should be the total velocity relative to the blade, but not including velocities induced by the blade itself since a lifting line representation is used. This means that CFD and experimental results can not be implemented easily, but the blade element momentum method can be used to generate input data effectively because the induction factors corresponds to the wake induced velocities on a flat blade. In the following, data for the flat reference blade presented in section 4.5 will be used as input.

The design method is based on the assumption that the winglet is relatively small and that only the circulation distribution on the outermost part of the blade is altered when winglets are attached to the flat reference blade. In practice the winglet geometry and the bound circulation will be defined and the velocities on the new geometry will be calculated. The definition of the bound circulation and the calculation of the new velocity distribution is described in detail in the following sections.

5.1 Defining Bound Circulation

The bound circulation used as input is defined over spanwise positions of the blade in the range $y/R \in [0, 1]$. On the blade with winglet this will be altered and extended onto the winglet using an appropriate scheme. If the design method described here is to be used it is necessary to keep the bound circulation constant until a position close to the tip (=y_0). On physical grounds the circulation-value, Γ_0, and the derivative , Γ_0', must be continuous at this point, because the force distribution is expected to vary smoothly. It will also be required that the circulation approaches zero at the winglet tip. The definitions are shown in Figure 5.1.a . Since the y-coordinate is not suited to describe non-flat blades the spanwise surface parameter s is used. s_0 corresponds to the y_0/R position and s >1 corresponds to positions on the winglet. Figure 5.1.b shows an example of a circulation distribution extended from s_0/R=0.91 onto a 3% winglet. A second parameter $s_t \in [0, s_{tip}]$ has also been defined, which descripes the part of the blade where the bound circulation is defined

$$s_t = s - s_0$$

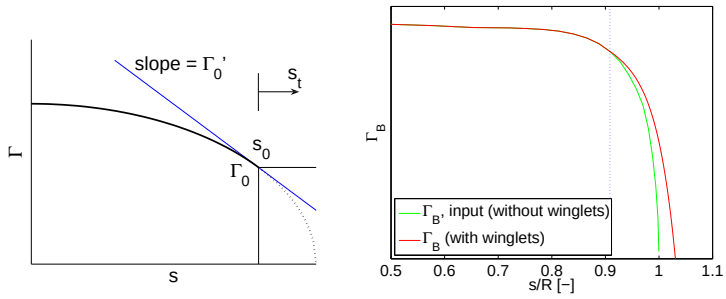

(a) Definitions of circulation parameters.

(b) Example of Γ_B with and without winglets.

Figure 5.1: Circulation distributions.

A systematic choice of the tip circulation $\Gamma_{tip}(s_t)$ is described in the following.. The tip circulation must satisfy the 3 physical conditions.

1 The derivative at s_t=0 must be continuous.

$$\left.\frac{d\Gamma_{tip}}{ds_t}\right|_{s_t=0} = \frac{d\Gamma_B}{ds_t}$$

2 The value at s_t=0 must be Γ_0 .

$$\Gamma_{tip}|_{s_t=0} = \Gamma_0$$

3 The circulation decays to zero at the tip.

$$\Gamma_{tip}|_{s_t=s_{tip}} = 0$$

Suppose a function $f(s_t)$ has been defined that satisfies these conditions. In order to be able to shape it it is multiplied by a function $g(s_t)$

$$\Gamma_{tip}(s_t) = f(s_t)g(s_t) \tag{5.1}$$

Since f already fulfills the conditions on the tip circulation, g must satisfy the following

1 The derivative at s=0 must be zero.

$$\left.\frac{dg}{ds}\right|_{s=0} = 0$$

2 The function value at s=0 must be unity.

$$g|_{s=0} = 1$$

3 The function value at s_t=s_{tip} is arbitrary but must be finite.

Once a basis function f has been defined any function g, that satisfies the above can be used to shape the tip circulation distribution. f and g has been selected in order to resemble the results of section 3.5 where the optimum circulation distribution on wings was found. More specifically f and g has been selected as

$$f(s_t) = as_t^2 + bs_t + c$$
$$g(s_t) = e^{\alpha s_t^2}$$

α is a shaping parameter. The constants are given as

$$a = -\frac{bs_{tip} + c}{s_{tip}^2} \qquad b = \left.\frac{d\Gamma_B}{ds_t}\right|_{s_t=0} \qquad c = \Gamma_0$$

An example of the resulting circulation distribution is shown in Figure 5.2. Note that negative values of α pushes the circulation to the left, and positive values to the right onto the winglet. I.e. α represents how heavy the winglet is loaded and larger values corresponds to a heavier loading.

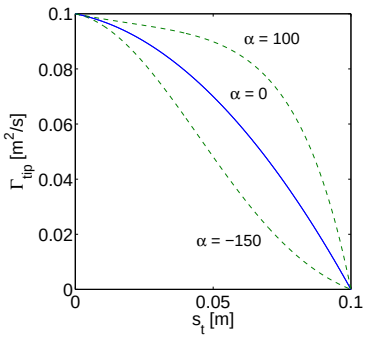

Figure 5.2: Examples of tip circulations against α-values.

5.2 Calculating Velocities

The velocities on the blade with winglet are needed in order to calculate the forces. The velocites are obtained by decomposing the input velocities on the flat blade into components that can be transfered onto the blade with winglet, taking into account the altered circulation distribution in the tip region. The wake is split into two parts, the nearwake and the farwake. The nearwake is the wake trailing of the outer part of the blade where the bound circulation is altered and one quarter revolution downstream. Figure 5.3 illustrates this. The farwake denotes all other wake singularites which includes the wake trailing of the inner part of the blade. The velocities induced by the farwake can be considered constant on the blade. To justify this, first consider the part of the farwake immediately behind the inner part of the blade. The wake strength is unchanged and assuming only small changes in the wake geometry, the induced velocities over the blade are also constant. Next consider the rest of the wake from the one quarter revolution and downstream. When the bound circulation near the tip is altered then so is the strength of the outermost part of the wake, but since the wake is a distance away from the blade the induced velocity on the blade is largely unaffected by this redistribution of wake strength.

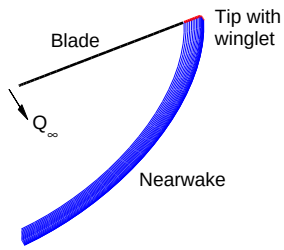

Figure 5.3: The nearwake extending one quarter revolution downstream.

The velocities at a given point on the blade is now assumed to consist of a constant part, $\mathbf{Q}_{FF}$, due to farwake induced and freestream velocities, and a part, $\mathbf{Q}_{NW}$, which is induced by the near wake and which depends on the distribution of bound circulation near the tip. $\mathbf{Q}_{NW}$ can be calculated based on the known strength and an assumed geometrical shape. If a helical shape is assumed the wake trailing of the position $\mathbf{x}=\{0, y, 0\}^T$ is described by

$$\mathbf{x}_{NW} = \{Q_\infty(1-a),\, y\cos t\Omega,\, -y\sin t\Omega\}^T \quad , t \in [0,\, \pi/(2\Omega)]$$

$\mathbf{Q}_{FF}$ can now be obtained on the main blade (i.e. not on the winglet) by subtracting $\mathbf{Q}_{NW}$ from the total velocity

$$\text{Blade:} \quad \mathbf{Q}_{FF} = \mathbf{Q} - \mathbf{Q}_{NW}$$

$\mathbf{Q}_{NW}$ should correspond to the input data of the flat blade. The winglet will be mounted along a line extending from the tip downstream. The velocity on this line is unknown except on the tip, $\mathbf{Q}_{tip}$, and can therefore be written as

$$\mathbf{Q} = \mathbf{Q}_{tip} + \Delta\mathbf{Q}_{FF} + \Delta\mathbf{Q}_{NW}$$

Where $\Delta\mathbf{Q}_{FF}$ and $\Delta\mathbf{Q}_{NW}$ denotes changes in $\mathbf{Q}_{FF}$ and $\mathbf{Q}_{NW}$ relative to $\mathbf{Q}_{tip}$. Even though $\mathbf{Q}_{FF}$ is constant on the blade this is not necessarily the case on the line where the winglet is mounted. Specifically, since the distance to the nearest downstream tip-vortices is relatively small when compared to the length of the winglet, the velocities induced thereby is expected to vary over the length of the winglet. $\Delta\mathbf{Q}_{FF}$, is modelled in section 5.2.1, and it is found to have a v-component. $\Delta\mathbf{Q}_{NW}$ can be calculated numerically as

$$\Delta\mathbf{Q}_{NW} = \mathbf{Q}_{NW} - \mathbf{Q}_{NW}|_{tip}$$

Subtracting $\mathbf{Q}_{NW}$ from $\mathbf{Q}$ yields the farfield induced velocities on the winglet

$$\text{Winglet:} \quad \mathbf{Q}_{FF} = \mathbf{Q}_{tip} + \Delta\mathbf{Q}_{FF} - \mathbf{Q}_{NW}|_{tip}$$

The constant velocity component $\mathbf{Q}_{FF}$ is now known over the blade with winglet. To obtain the total velocity it is necessary to add the nearwake induced velocity $\mathbf{Q}_{NW}$, but this should now be evaluated based on the defined bound circulation.

5.2.1 Modelling $\Delta \mathbf{Q}_{FF}$

To model the change in the farfield velocity along the winglet the wake singularities that are relatively close to it must be considered. This is mainly the wake trailing of the inner part of the blade and the downstream wake directly behind the blade tip. The former is parallel to the winglet and with constant distance, meaning that the induced velocities are relatively constant. The latter is expected to vary significantly over the winglet since it is directed perpendicular to it and the distance to it varies significantly over the winglet. In the following the wake downstream is assumed to consists of concentrated tip and root vortices. The strength of both is half the maximum value of the bound circulation

$$\Gamma = max(\Gamma_B)$$

Instead of simply modelling a large part of the wake numerically it will be shown that it is only necessary to take into account a small part of the wake. The final equation is written as a sum consisting of few terms, which can be included in analytical models. Figure 5.4 illustrates the important downstream tipvortices.

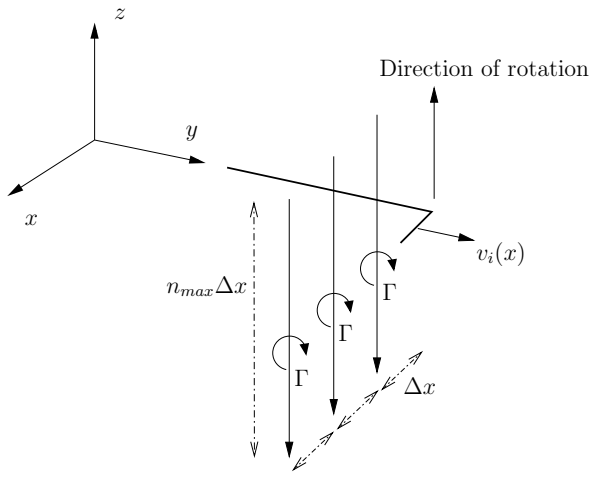

Figure 5.4:

The distance from the tip to the n'th downstream tipvortex is

$$\Delta x_n = \underbrace{Q_\infty (1-a)\frac{2/3\pi}{\Omega}}_{\Delta x} n$$

The ratio of turbine circumference to Δx is

$$\frac{\Delta x_n}{2\pi R} = \frac{1/3(1-a)}{\lambda} n$$

For a tip speed ratio of λ=8 the ratio is 1/28. I.e. the first tip vortex is 1/28 of the turbine circumference downstream. This is so close to the turbine that it must be expected that the induced velocity varies over the winglet. Therefore the influence of n_{max} downstream tipvortices must be included. To determine n_{max} a vortex segment of a tipvortex directly downstream of the tip is considered. The induced velocity on the winglet is in the positive y-direction and of magnitude

$$dQ_i(r) = \frac{\Gamma}{4\pi} \frac{1}{r^2} ds$$

The ratio of induction at the tip and the root of the winglet is (assuming an axial induction of 1/3)

$$\alpha = \frac{dQ_i(\Delta x_n - h)}{dQ_i(\Delta x_n)} = \frac{1}{1 - \frac{h}{4Rn\pi/(9\lambda)}}$$

Specifying α and solving for n yields n_{max}. E.g. α=1.10 $\Rightarrow$ n_{max}=4, i.e. by including 4 downstream tipvortices, the induced velocity over the winglet by any vortex constituting the farwake, will vary less or equal to 10%. Since most of the tip-vortices are at large distances from the winglet, only a part of it with a length equal to the distance downstream of the n_{max}'th tip vortex, will be modelled. This is 11% of the rotor circumference and the circular shape can be approximated as a straight line vortex. The induced velocity of such a straight tip vortex segment of length $\Delta x\, n_{max}$ on the winglet can be written using (2.7) as

$$v_i(x,n) = \frac{\Gamma}{2\pi(\Delta x\, n - x)} \left(\cos\left(\tan^{-1}\left(\frac{2(n - x/\Delta x)}{n_{max}} \right) \right) \right)$$

The velocity is in the positive outward radial direction. The induced velocity due to the n_{max} tip vortex segments is

$$v_i(x) = \sum_{n=1}^{n_{max}} v_i(x,n)$$

Finally, the change in the farfield induced velocity relative to the velocity at the tip is

$$\Delta \mathbf{Q}_{FF} = \{0, v_i(x) - v_i(0), 0\}^T$$

Figure 5.5 shows ΔQ_{FF} over a 5% winglet. The velocity increases to 6% of Q_∞, which is not substantial but can be expected to have an influence.

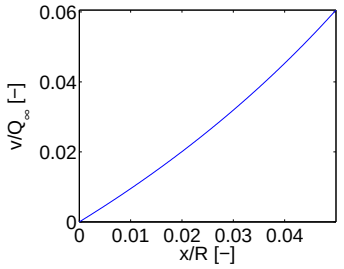

Figure 5.5: The v-component of $\Delta\mathbf{Q}_{FF}$.

5.3 Summary of Method

The velocity over the blade with winglet can now be found by calculating the velocities induced by the nearwake on all blade and winglet stations and adding it to the farfield velocity field. The forces are evaluated on the lifting line using the method described in section 3.7. The complete algorithm is described below.

- Select a point close to the tip, y_0, and determine Γ_0 and Γ_B.
- Define a tip geometry based on winget height, h/R.
- Calculate the farfield velocities on the blade and winglet, $\mathbf{Q}_{FF}$.
- Assume a tip circulation distribution.
- Calculate nearwake strength and shape.
- Calculate nearwake induced velocities on blade and winglet, $\mathbf{Q}_{NW}$.
- Calculate total velocity on blade and winglet, $\mathbf{Q}$=$\mathbf{Q}_{NW} + \mathbf{Q}_{FF}$.
- Evaluate forces based on the total velocity and defined bound circulation distribution.
- Define twist and chord according to velocity and bound circulation distribution.

5.4 Validation

The method can not be fully evaluated because no data for comparison is at hand. Here it will be shown that the method is consistent and the sensitivity of important parameters will be discussed.

5.4.1 Convergence with respect to discretization.

n_c denotes the number of collocation points on the tip. They are distributed according to a cosine spacing scheme (equation (3.1)) in the range $s_t \in [0, s_{tip}]$. A parameter study has been made using data from table 5.1. Figure 5.6 illustrates how the C_P-values converges when plotted against $1/n_c$. An infinitely large discretization is equivalent to $1/n_c$=0 and the assumed exact result is read of as C_P=0.5269. Comparing this with the results it is found that the results are within 99.90% of the exact value for $n_c \geq$80. n_{qw} is the number of vortices in óne trailing nearwake vortex. The results depends very little on this number and a low value is sufficient.

n_{qw}=20	$n_c \in [30, 100]$	$x_{t1}=\pi/2$	x_{t2}=0
h/R=0.032	R_c/h=0.10	y_0/R=0.9085	$\Gamma_0/(Q_\infty R)$=0.1068
C_l/C_d = 110	a=1/3	α=83.33	

Table 5.1: Parameters used for studying variation of n_c.

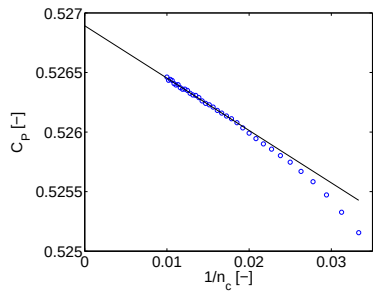

Figure 5.6: Convergence of C_P against $1/n_c$.

5.4.2 Influence of assumed axial induction, a.

The influence of the choice of a is not obvious, since it affects both the inflow velocity and the shape of the wake. A parameter study using data from table 5.2 shows that the results are largely unaffected of varying its value. Figure 5.7 shows how the C_p values depends on a.

n_{qw}=20	n_c=80	$x_{t1}=\pi/2$	x_{t2}=0
h/R=0.032	R_c/h=0.10	y_0/R=0.9085	$\Gamma_0/(Q_\infty R)$=0.1068
C_l/C_d = 110	$a \in [1/4, 1/2]$	α=83.33	

Table 5.2: Parameters used for studying variation of a.

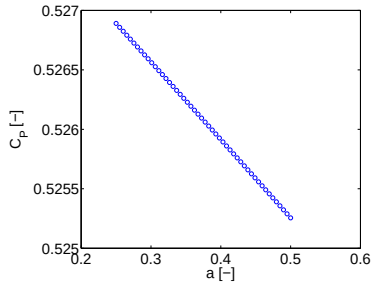

Figure 5.7: Dependency on variation of a.

5.4.3 Influence of choice of y_0.

The choice of y_0 influences many parameters and therefore it is hard to study the effect of varying it. Selecting a value very close to the tip means that the circulation that can be distributed onto the winglet is very small, hence decreasing the potential effect of it. The optimum choice would be to select a value where the tip effects are not yet dominating the circulation distribution. In practice this means that Γ_0 should have a relatively large value and that Γ_0 should be relatively small, but the freedom of choice is still limited by the condition that the farwake must be considered unaffected. In practice it is found that good results can be obtained by setting $y_0 \approx$0.85-0.90.

Figure 5.8 illustrates the problem. For different values of y_0/R the optimal value of α and therefore C_p is found. The C_p value apparently increases when y_0/R decreases but the results are uncertain because the farfield of the wake can then no longer be assumed to be unaffected.

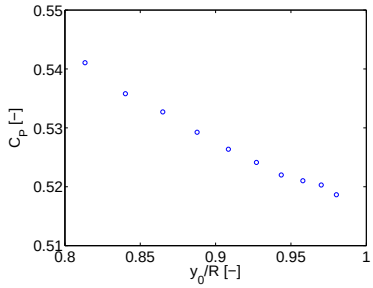

Figure 5.8: The optimized C_p values for different choices of y_0/R .

5.4.4 Influence of Curve Radius R_c/h .

In this study the optimal value of α is found for each value of the curve radius R_c/h. Parameters are given in table 5.3. Figure 5.9 shows how the largest C_p values are found for small curve radii. This result is consistent with the results for the optimum loaded wing given in section 3.5.

n_{qw}=20	n_c=80	x_{t1}=$\pi/2$	x_{t2}=0
h/R=0.032	$R_c/h \in$[0.05, 0.50]	y_0/R=0.90	$\Gamma_0/(Q_\infty R)$=0.1068
C_l/C_d = 110	a=1/3	α=$\alpha(R_c/h)$	

Table 5.3: Parameters used for studying variation of R_c/h.

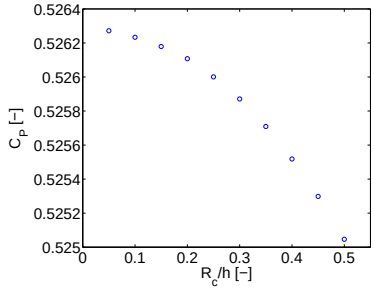

Figure 5.9: Influence of varying curve radius, R_c/h .

5.5 General Design Results

In this section the influence of the shaping parameter α and the winglet height are studied. Based on the parameters in table 5.4 the power and thrust coefficients has been calculated for 40 values of h/R and α.

n_{qw}=20	n_c=80	$x_{t1}=\pi/2$	x_{t2}=0
$h/R \in$[0.01, 0.07]	R_c/h=0.10	y_0/R=0.8878	$\Gamma_0/(Q_\infty R)$=0.1068
C_l/C_d = 110	a=1/3	$\alpha \in$[-50, 200]	

Table 5.4: Table of parameters.

Figure 5.10 shows a contour plot of the C_p values. The maximum C_p is found for a winglet height of approximately 3.5% and α=75. If α is increased further the C_p values decreases fast. This is because the viscous drag associated with the heavier loading of the winglet starts to dominate. For larger winglets this happens for smaller values of α.

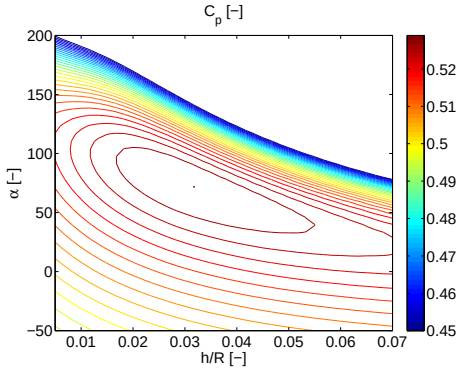

Figure 5.10: Calculated power coefficients.

Figure 5.11 shows only the range of C_p values larger than the values for a flat blade. Note that only a band of α values yields an increase in C_p, and therefore that only well designed winglets contributes positively.

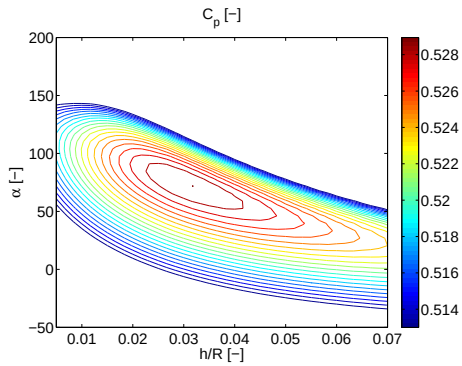

Figure 5.11: The range of increased C_p relative to flat wing

The thrust coefficients are shown in Figure 5.12. As expected they increases with increasing α values, because the loading on the winglet and the outer part of the blade increases.

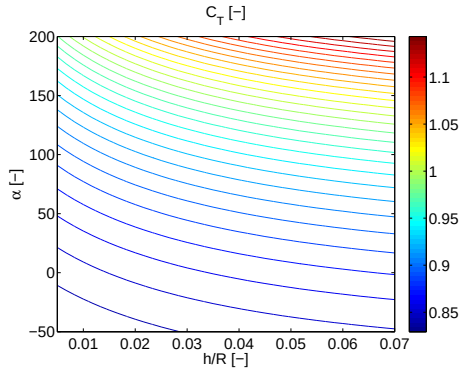

Figure 5.12: Calculated thrust coefficients

A large increase in thrust is unwanted and therefore is it not possible to point out the best design. Figure 5.13 shows a contour plot of the ratios of power to thrust (C_p/C_T). A large value is desired but this is not possible without selecting a C_p lower than the maximum possible. On the figure is also shown with black the contour lines corresponding to C_p values of 0.52 and 0.528 respectfully. They show that choosing the optimum C_p value (C_p=0.528) corresponds to a low value of (C_p/C_T), and therefore a large C_T. Choosing C_p=0.52 instead is possible without an associated large increase in thrust. Two sets of h/R and α values has been selected based on this and these designs will be threated in

detail in part 6. They are denoted optimum and conservative design respectfully. Table 5.13 summaries their parameters. Note that a third, interesting design is found for a winglet height of h/R=0.02 and α=50. This winglet is small with a relatively high C_p value, and an increase in thrust which lies between the conservative and the optimum design values. Due to time limitations it will not be threated further.

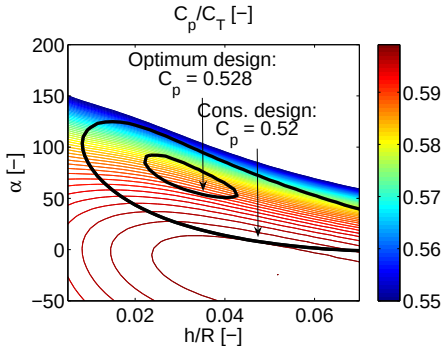

Figure 5.13: Ratio of C_p to C_T and the choices of conservative and optimum design.

Conservative design	C_p=0.521	C_T=0.871
	α=7.69	h/R= 0.048
Optimum C_p design	C_p=0.528	C_T=0.892
	α=52.56	h/R=0.035

Table 5.5: Design parameters for defined conservative and optimum design.

5.6 Conclusions

Using the described design algorithm important general design conclusions has been established. Especially how the winglet height and the bound circulation influences the overall design. Based on this two designs has been defined which will be studied in part 6.

The design algorithm is fast. One evaluation of a design takes approximately 1 second in Matlab using a fully numerical code which is not optimized. More efficient coding in C or Fortran can substantially decrease the computational time, and this makes the model fast enough for implementation in an unsteady BEM algorithm.

Part 6

Final Designs

A conservative and an optimum winglet design is described in detail. The design parameters are based on the discussion in section 5.5. Unless otherwise stated the results are calculated using the design algorithm described in part 5 using the flat blade reference data of section 4.5 as input.

6.1 Conservative Winglet Design

Design parameters are given in table 6.1.

n_{qw}=20	$n_c \in$80	$x_{t1}=\pi/2$	x_{t2}=0
h/R=0.048	R_c/h=0.10	y_0/R=0.8878	$\Gamma_0/(Q_\infty R)$=0.11083
C_l/C_d = 110	a=1/3	α=7.69	λ=8

Table 6.1: Design parameters for 4.8% conservative winglet design.

6.1.1 Overall Design Results

Table 6.2 summaries the geometry and performance parameters. Notice that the C_p value is increased by 1.60% for a 0.65% increase in thrust relative to a flat blade.

h/R	R_c/h	C_p	C_T
0.048	0.10	0.521 (+ 1.60 %)	0.871 (+ 0.65%)

Table 6.2: Final design results

The calculated wake induced velocities and the bound circulation distribution over the blade is seen in figure 6.1.a and 6.1.b. Note the large negative v-velocity component, in the direction from the winglet towards the hub. This is desirable because it decreases the normalwash on the winglet. The circulation is distributed smoothly onto the winglet and differs from the flat blade only in a region very close to the winglet. This shape is physically realistic and because the changes are confined to a very small region the assumptions in the design algorithm are expected to be fullfiled.

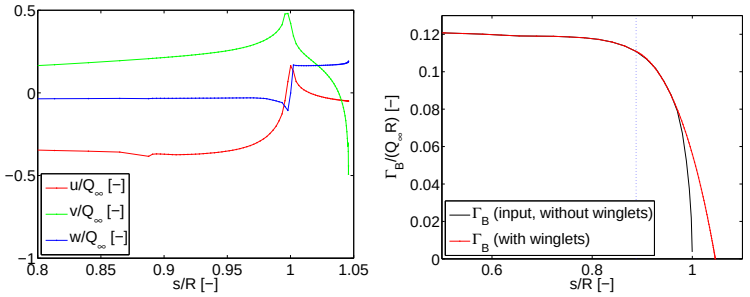

(a) Wake induced velocities (b) Bound circulation

Figure 6.1: Induced velocities and bound circulation.

The twist and chord distribution on the outer part of the blade and the winglet is shown in Figure 6.2 and the blade itself is seen in figure 6.3. The blade is designed using the Risø-B118 profile at 8 degrees angle of attack.

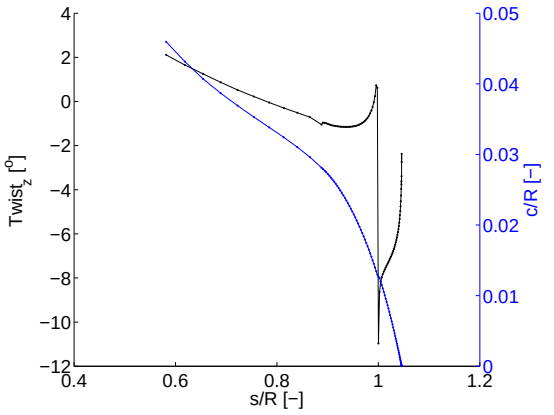

Figure 6.2: Twist and chord distribution on outer part of blade.

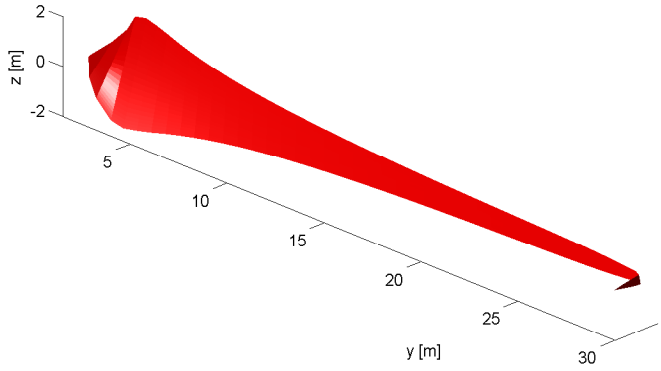

Figure 6.3: The final blade with winglet.

6.1.2 Design Predicted Performance

The section C_p values over the blade are shown in Figure 6.4. The inviscous (Joukowsky) forces on the winglet contributes with negative values and the winglet is therefore being dragged by the main blade. The winglet is relatively slim and is lightly loaded on the outer part. Because it is desirable to have a low winglet height this design can probably be improved by using a smaller winglet with heavier loading.

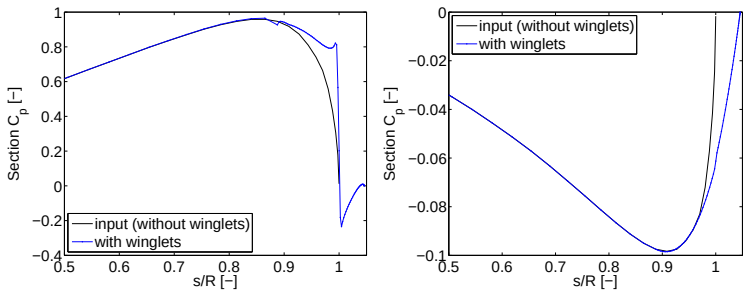

(a) Joukowsky forces. (b) Viscous forces.

Figure 6.4: Section C_p due to Joukowsky (lift) and Viscous forces.

The section thrust coefficient distribution is shown in figure 6.5. There is only a very small increase in thrust forces near the tip. Notice that the winglet itself is not subject to thrust forces.

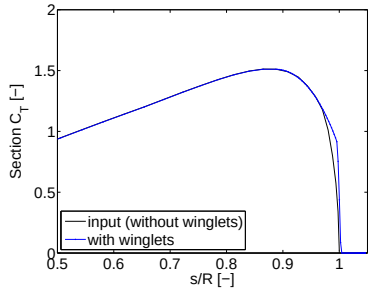

Figure 6.5: Section thrust coefficients

The normalwash on wind turbines, Q_n, is defined in Figure 6.6 as the component of the total velocity perpendicular to both the blade lifting line and the direction of rotation. It is defined positive in the direction from the suction to the pressure side, and is the velocity component responsible for the generation of torque according to the Joukowsky theorem. Notice that positive values generates negative torque, and it is therefore desirable that Q_n is decreased relative to the flat blade.

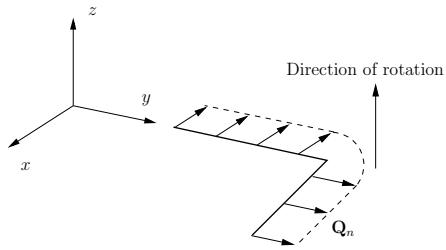

Figure 6.6: Definition of normalwash on a wind turbine blade.

Figure 6.7 shows the calculated normalwash. On the main blade the normalwash has been decreased near the tip, which is important because it decreases the induced drag. The normalwash on the winglet is positive and it yields a negative contribution to the power production.

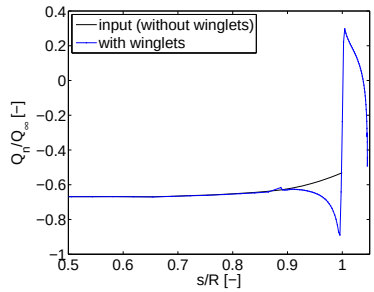

Figure 6.7: Normalwash velocity magnitude.

6.1.3 Vortex Lattice Simulation Results

Using the free wake vortex lattice code the power and thrust coefficients are C_p=0.534 and C_T=0.916. This is an increase of 0.6% and 3.8% respectively, relative to the vortex lattice results for the flat blade given in table 4.5. This is not in agreement with the results of the design algorithm stated above. Figure 6.8.a compares the calculated bound circulation with the design goal. There is some agreement but the relative error is large. Figure 6.8.b shows the section C_p values due to the Joukowsky forces on the blade. The agreement is not good. One source of error is the relatively coarse grid near the tip of the blade which can not resolve the distribution of properties accurately. Due to excessive computational time it is not possible to increase it and it was therefore decided to make no further vortex lattice simulations.

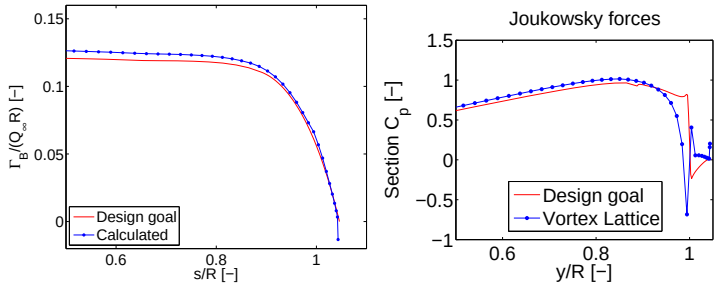

(a) The bound circulation distribution.

(b) The section C_p due to Joukowsky forces.

Figure 6.8: Vortex lattice simulation results compared to design values.

6.2 Optimum Winglet Design

Design parameters are given in table 6.3.

n_{qw}=20	n_c ∈80	$x_{t1}=\pi/2$	x_{t2}=0
h/R=0.035	R_c/h=0.10	y_0/R=0.8878	$\Gamma_0/(Q_\infty R)$=0.1108
C_l/C_d = 110	a=1/3	α=52.56	λ=8

Table 6.3: Design parameters for 3.5% optimum winglet design.

6.2.1 Overall Design Results

Table 6.9 summaries the geometry and performance parameters. Notice that the C_p value is increased by 2.9% but the increase in thrust relative to a flat blade is now relatively large, 3.1%.

h/R	R_c/h	C_p	C_T
0.035	0.10	0.528 (+ 2.9 %)	0.892 (+ 3.1%)

Table 6.4: Design parameters for 3.5% optimum winglet design.

The calculated wake induced velocities and the circulation distribution over the blade is seen in figure 6.9.a and 6.1.b. The circulation differs substantially from the conservative design, i.e. the outer part of the blade and the winglet is now heavily loaded.

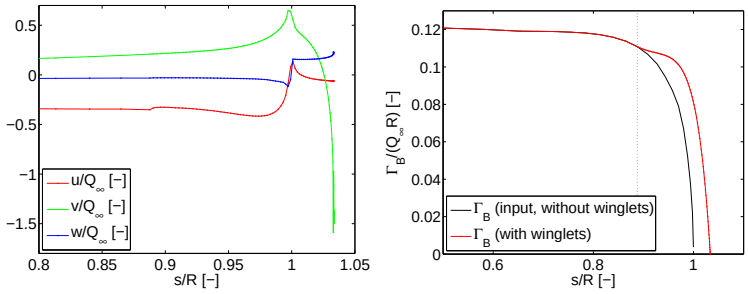

(a) Wake induced velocities (b) Bound circulation

Figure 6.9: Induced velocities and bound circulation.

The twist and chord distribution on the outer part of the blade and the winglet is shown in Figure 6.10 and the blade itself is seen in figure 6.11. The blade is designed using the Risø-B118 profile at 8 degrees angle of attack.

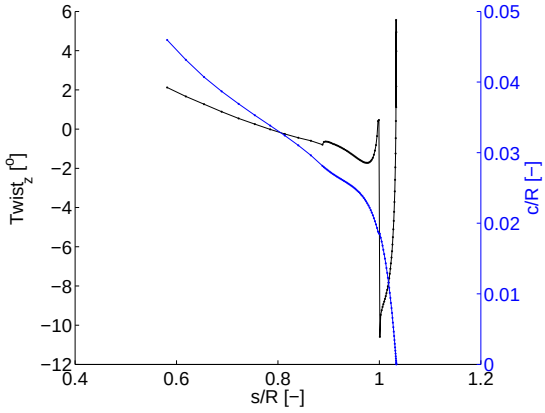

Figure 6.10: Twist and chord distribution on outer part of blade.

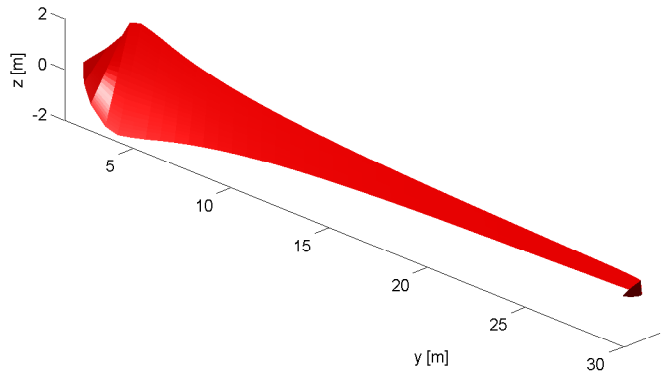

Figure 6.11: The final blade with winglet.

6.2.2 Design Predicted Performance

The section C_p values over the blade are shown in Figure 6.4. The winglet is being dragged by the main blade and the viscous forces are increased substantially due to the heavier loading of the outer part of the blade and the winglet.

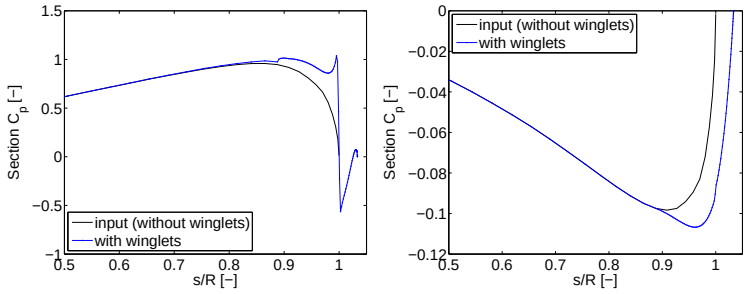

(a) Joukowsky forces.

(b) Viscous forces.

Figure 6.12: Section C_p due to Joukowsky (lift) and Viscous forces.

The section thrust coefficient distribution is shown in figure 6.13. There is now a large increase in thrust near the tip, and this indicates that the increase in C_p is caused mainly by the large forces near the tip.

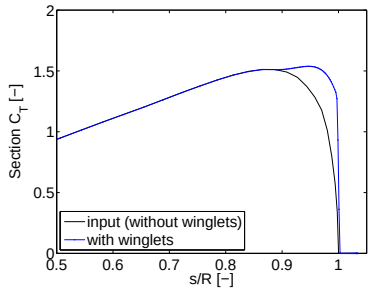

Figure 6.13: Section thrust coefficients

Figure 6.14 shows the normalwash. The reduction is small compared to the conservative design, and this confirms that the large increase in C_p is due to the larger forces near the tip.

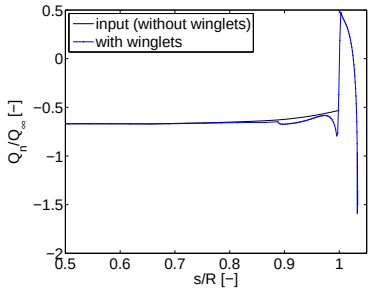

Figure 6.14: Normalwash velocity magnitude.

6.3 Conclusions

The distributed properties calculated using the design algorithm are physically reasonable and indicates very well how the winglet affects the tip region. The vortex lattice results are not in agreement with the design algorithm. This can be caused by the numerous problems already described, or it can be caused by the poor discretization of the winglet. It is also a possibility that the design algorithm is not correct, and at this point it is desirable to make a CFD validation before progressing further.

The physics of the two designs confirms the general design conclusions of section 5.5.

Part 7

Conclusion

The implemented vortex lattice and panel code were not satisfactory. Among other issues the problems were related to uncertainties in the free wake model and excessive computational time. The latter implicated that a relatively coarse discretization had to be used which further added to the uncertainty of the results.

The developed design method is fast and consistent. It can predict the change in flow properties near the tip and the associated forces introduced by the winglet. The method have not yet been validated, something which the vortex lattice code was intended for, but the results are physically reasonable and comparable to other results reported in the literature. The design method is based on the decomposition of the total velocity into a constant component and a nearwake induced component. This approach appears promising and can form the basis for aeroelastic computations.

Winglets was found to affect only the outermost part of a wind turbine blade ($y/R >\approx 0.85$) indicating that it affects the flow locally. The induced drag component is decreased in this region but the thrust forces are increased. A general design study has shown that it is possible to design for a large increase in power with a relatively small associated increase in thrust forces relative to a flat blade of the same radius. I.e. an increase in C_p of 1.65% for an increase in C_T of 0.65%. The power can be increased by as much as 2.9% but the increase

in C_T is then 3.1%. It was further shown that winglets of a given height can have both a positive and a negative effect depending on the distributed loading. I.e. winglets has to be well designed. Winglet with heights in the range of 2-4% of the rotor radius appears to be most effective.

Appendix A

Appendix

A.1 Constant Strength Source Panel (3 Nodes)

A solution to (2.8) in closed form for both the induced potential and the velocity of a 4 node constant strength sourcepanel is given in Katz[11]. Often a 3 point panel is required and the transformation to a 3 point panel is described below. The transformation is based on equations (10.95) - (10.97) in Katz[11] which are not stated here. The final set of equations will be stated below. Notice that the panel is entirely in a x-y plane and therefore a transformation of coordinates and of the resulting induced velocity is required in practical applications.

A.1.0.1 Transformation of 4 Node Constant Strenght Source Panel Into 3 Node Panel

set (x_3, y_3)=(x_4, y_4). This yields

$$\begin{aligned} d_{34} &= 0 \\ d_{41} &= d_{31} \\ m_{41} &= m_{31} \\ r_3 &= r_4 \\ e_3 &= e_4 \\ h_3 &= h_4 \end{aligned}$$

Notice that m_{34} is undefined, but all terms including it cancels since

$$\tan^{-1}\left(\frac{m_{34}e_3 - h_3}{zr_3}\right) = \tan^{-1}\left(\frac{m_{34}e_4 - h_4}{zr_4}\right)$$

It remains to find the limit of the following 2 terms as $(x_3, y_3) \to (x_4, y_4)$

$$\frac{y_4 - y_3}{d_{34}} \ln\left(\frac{r_3 + r_4 - d_{34}}{r_3 + r_4 + d_{34}}\right) \tag{A.1}$$

$$\frac{x_3 - x_4}{d_{34}} \ln\left(\frac{r_3 + r_4 - d_{34}}{r_3 + r_4 + d_{34}}\right) \tag{A.2}$$

Substituting d_{34} into (A.1) and rewriting it yields

$$\begin{aligned} &\frac{y_4 - y_3}{\sqrt{(x_4 - x_3)^2 + (y_4 - y_3)^2}} \ln\left(\frac{r_3 + r_4 - d_{34}}{r_3 + r_4 + d_{34}}\right) \\ &= \underbrace{\sqrt{\frac{1}{\frac{(x_4 - x_3)^2}{(y_4 - y_3)^2} + 1}}}_{\in[1, 0^+]} \underbrace{\ln\left(\frac{r_3 + r_4 - d_{34}}{r_3 + r_4 + d_{34}}\right)}_{\to \ln(1)=0} \end{aligned}$$

The argument to the logarithm is 1 in the limit since d_{34} goes to zero and r_3=r_4 is finite. In the limit $\frac{(x_4 - x_3)^2}{(y_4 - y_3)^2}$ can take the values $[0, +\infty]$. Therefore the square root is limited and takes values in the range $[1, 0^+]$. Muliplying this with ln(1)=0 gives the result that the whole term is zero. By the same argumentation (A.2) is equal to zero.

A.1.0.2 Velocity Induced by a 3 Node Constant Strength Source Panel

The equations describing the velocity induced at point (x, y, z) by a 3 point source panel of strength σ (Figure 2.6), is stated below. Notice that the panel must lie in the x-y plane. I.e. the nodes must have the coordinates $(x_1, y_1, 0)$, $(x_2, y_2, 0)$ and $(x_3, y_3, 0)$.

$$
\begin{aligned}
d_{12} &= \sqrt{(x_2 - x_1)^2 + (y_2 - y1)^2} \\
d_{23} &= \sqrt{(x_3 - x_2)^2 + (y_3 - y2)^2} \\
d_{31} &= \sqrt{(x_1 - x_3)^2 + (y_1 - y3)^2} \\
m_{12} &= \frac{y_2 - y_1}{x_2 - x_1} \\
m_{23} &= \frac{y_3 - y_2}{x_3 - x_2} \\
m_{31} &= \frac{y_1 - y_3}{x_1 - x_3} \\
r_k &= \sqrt{(x - x_k)^2 + (y - y_k)^2 + z^2} \quad , k = 1, 2, 3 \\
e_k &= (x - x_k)^2 + z^2 \quad , k = 1, 2, 3 \\
h_k &= (x - x_k)(y - y_k) \quad , k = 1, 2, 3
\end{aligned}
$$

The induced velocity components:

$$
\begin{aligned}
u =& \frac{\sigma}{4\pi} \left[\frac{y_2 - y_1}{d_{12}} \ln \frac{r_1 + r_2 - d_{12}}{r_1 + r_2 + d_{12}} + \frac{y_3 - y_2}{d_{23}} \ln \frac{r_2 + r_3 - d_{23}}{r_2 + r_3 + d_{23}} + \frac{y_1 - y_3}{d_{31}} \ln \frac{r_3 + r_1 - d_{31}}{r_3 + r_1 + d_{31}} \right] \\
v =& \frac{\sigma}{4\pi} \left[\frac{x_1 - x_2}{d_{12}} \ln \frac{r_1 + r_2 - d_{12}}{r_1 + r_2 + d_{12}} + \frac{x_2 - x_3}{d_{23}} \ln \frac{r_2 + r_3 - d_{23}}{r_2 + r_3 + d_{23}} + \frac{x_3 - x_1}{d_{31}} \ln \frac{r_3 + r_1 - d_{31}}{r_3 + r_1 + d_{31}} \right] \\
w =& \frac{\sigma}{4\pi} \left[\tan^{-1} \left(\frac{m_{12} e_1 - h_1}{z r_1} \right) - \tan^{-1} \left(\frac{m_{12} e_2 - h_2}{z r_2} \right) + \right. \\
& \tan^{-1} \left(\frac{m_{23} e_2 - h_2}{z r_2} \right) - \tan^{-1} \left(\frac{m_{23} e_3 - h_3}{z r_3} \right) + \\
& \left. \tan^{-1} \left(\frac{m_{31} e_3 - h_3}{z r_3} \right) - \tan^{-1} \left(\frac{m_{31} e_1 - h_1}{z r_1} \right) \right]
\end{aligned}
$$

Bibliography

[1] John D. Anderson. *Fundamentals of Aerodynamics*. 2005.

[2] Jr Clarence D. Cone. The theory of induced lift and minimum induced drag of nonplanar lifting systems, nasa r-139. 1962.

[3] Eppler. Induced drag and winglets. 1995.

[4] Maughmer et. al. The design and testing of a winglet airfoil for low speed aircraft. 2001.

[5] Mac Gaunaa and Jeppe Johansen. Can Winglets Increase Cp. 2007.

[6] Stig Øje. Instationære aerodynamiske kræfter på todimensionalt vingeprofil. 1980.

[7] Kroo. Drag due to lift. concepts for prediction and reduction. 2000.

[8] Jones & Lasinsky. Effect of winglets on the induced drag of ideal wing shapes. 1980.

[9] Maughmer. The design of winglets for high-performance sailplanes. 2001.

[10] Jack Moran. *Theoretical and Computational Aerodynamics*. 1984.

[11] Katz & Plotkin. *Low Speed Aerodynamics*. 2005.

[12] Jeppe Johansen & Niels N. Sørensen. Aerodynamic investigation of winglets on wind turbine blades using cfd. 2006.

[13] Gijs Van Kuik Tonio Sant and G. J. W. van Bussel. Estimating the angle of attack from blade pressure measurements on nrel phase vi rotor using a free wake vortex model: Axial conditions. 2006.

Risø's research is aimed at solving concrete problems in the society.

Research targets are set through continuous dialogue with business, the political system and researchers.

The effects of our research are sustainable energy supply and new technology for the health sector.